MNRAS 000, 1–21 (2026) Preprint 3 August 2026 Compiled using MNRAS LaTeX style file v3.2

Misaligned or chaotic? A strong break of axial symmetry in the local LRD J1025 revealed with VLT/FORS2 spectropolarimetry

Francesco D'Eugenio [1,2⋆†], Gabriele Pezzulli [3⋆‡], Roberto Maiolino [1,2,4], Alessandro Marconi [5,6], Xihan Ji [1,2], Cristina Ramos Almeida [7,8], Andrea Ferrara [9], Piero Madau [10], Xiaojing Lin [11,12], José A. Acosta-Pulido [7,8], Fuyan Bian [13,14], Matilde Brazzini [15,16,14,1,2], Zheng Cai [11], Stefano Carniani [9], Xiaohui Fan [12], Ignas Juodžbalis [1,2], Robert G. Pascalau [1,2], Jan Scholtz [1,2], Charlotte Simmonds [17], Fengwu Sun [18], and Sandro Tacchella [1,2]

[1] *Kavli Institute for Cosmology, University of Cambridge, Madingley Road, Cambridge CB3 0HA, UK*
[2] *Cavendish Laboratory, University of Cambridge, JJ Thomson Avenue, Cambridge CB3 0HE, UK*
[3] *Kapteyn Astronomical Institute, University of Groningen, Landleven 12, 9747 AD Groningen, The Netherlands*
[4] *Department of Physics and Astronomy, University College London, Gower Street, London WC1E 6BT, UK*
[5] *Dipartimento di Fisica e Astronomia, Università degli Studi di Firenze, Via G. Sansone 1, 50019 Sesto Fiorentino (Firenze), Italy*
[6] *INAF – Osservatorio Astrofisico di Arcetri, Largo E. Fermi 5, 50125 Firenze, Italy*
[7] *Instituto de Astrofísica de Canarias, Calle Vía Láctea s/n, E-38205 La Laguna, Tenerife, Spain*
[8] *Departamento de Astrofísica, Universidad de La Laguna, E-38206 La Laguna, Tenerife, Spain*
[9] *Scuola Normale Superiore, Piazza dei Cavalieri 7, 56126 Pisa, Italy*
[10] *Department of Astronomy and Astrophysics, University of California, Santa Cruz, 1156 High Street, Santa Cruz, CA 95064, USA*
[11] *Department of Astronomy, Tsinghua University, Beijing 100084, China*
[12] *Steward Observatory, University of Arizona, 933 N. Cherry Avenue, Tucson, AZ 85721, USA*
[13] *European Southern Observatory, Alonso de Córdova 3107, Casilla 19001, Vitacura, Santiago 19, Chile*
[14] *Chinese Academy of Sciences South America Center for Astronomy, National Astronomical Observatories, CAS, Beijing 100101, People's Republic of China*
[15] *Dipartimento di Fisica, Sezione di Astronomia, Università degli Studi di Trieste, Via G.B. Tiepolo 11, 34143 Trieste, Italy*
[16] *INAF – Osservatorio Astronomico di Trieste, Via G. B. Tiepolo 11, I-34143 Trieste, Italy*
[17] *Departamento de Astronomía, Universidad de Chile, Camino El Observatorio 1515, Las Condes, Santiago, Chile*
[18] *Center for Astrophysics | Harvard & Smithsonian, 60 Garden Street, Cambridge, MA 02138, USA*

Accepted XXX. Received YYY; in original form ZZZ

ABSTRACT

Little Red Dots (LRDs) are compact active galactic nuclei (AGN) with unusual spectral energy distributions and broad Balmer emission, candidate signposts of rapid black-hole growth. We present VLT/FORS2 optical linear spectropolarimetry of the closest known LRD, SDSS J102530.29+140207.3, at $z = 0.1$. In total light, we detect spatially extended narrow-H α emission, probably tracing the host galaxy. We measure a nearly grey continuum polarisation $p_{\rm cont} = 1.53 \pm 0.04({\rm rand.}) \pm 0.20({\rm syst.})$ per cent, while broad H α is less polarised, $p_{\rm H\alpha} = 0.58$–0.84 per cent. We rule out polarisation by Milky Way dust and dilution by an unpolarised line. The polarised continuum with a depolarised line resembles local Seyfert-1 nuclei and favours a single dominant source over multi-source explanations. After Stokes-continuum subtraction, broad H α shows no blue-to-red swing, but there is a significant $(48 \pm 4)°$ continuum-to-line offset in polarisation angle. This implies a break of axial symmetry inside this object, posing interesting geometrical challenges to all existing LRD models and frameworks. We discuss different possible origins of this symmetry break and possible paths to discriminate between them with future observations.

Key words: galaxies: active – galaxies: nuclei – galaxies: Seyfert – polarisation – radiative transfer

1 INTRODUCTION

JWST has uncovered a populous class of compact, optically red sources at $z \gtrsim 4$ showing broad Balmer (and often He) emission and a characteristic 'V-shaped' UV–optical continuum, dubbed 'Little Red Dots' (LRDs; Matthee et al. 2024; Greene et al. 2024; Kocevski et al. 2025). Their physical nature is still debated, because several of their properties are atypical for standard unobscured active galactic nuclei (AGN). They are strong in the optical, but weak at wavelengths where AGN often dominate: X-rays (Simmonds et al. 2016; Yue et al. 2024; Ananna et al. 2024; Lambrides et al. 2026b; Pacucci & Loeb 2024; Maiolino et al. 2025), high-ionization lines (Lambrides et al. 2026b; Zucchi et al. 2026; Wang et al. 2026; Ji et al. 2026c), mid-infrared (MIR; Akins et al. 2025; Setton et al. 2025a; Barro

⋆ These authors contributed equally to the article.
† E-mail: francesco.deugenio@gmail.com
‡ E-mail: pezzulli@astro.rug.nl

et al. 2025; Ronayne et al. 2026; Leung et al. 2025; Wang et al. 2025, but see also Delvecchio et al. 2025; Brazzini et al. 2026), and radio (Mazzolari et al. 2026). They also host black holes that seem to be 'overmassive' relative to their host stellar mass and to the expectation set by the local black-hole mass–stellar-mass relation ($M_\bullet$–$M_\star$; Harikane et al. 2023; Maiolino et al. 2024; Greene et al. 2024; Taylor et al. 2025; Juodžbalis et al. 2026a; Jones et al. 2025).

Noticing that a significant fraction of LRDs are characterised by exponential wings in their broad-line profiles, it has been proposed that the width of the broad Balmer lines arises primarily from electron scattering in dense ionized gas (Rusakov et al. 2026), which would imply substantially narrower intrinsic line widths and hence much smaller $M_\bullet$. The electron scattering interpretation is attractive for two reasons. First, because it naturally explains the exponential wing shape in many LRDs (Rusakov et al. 2026; Torralba et al. 2026; Matthee et al. 2026); second, by lowering $M_\bullet$, it resolves the problem of overmassive black holes (Maiolino et al. 2024)[1], while implying a rapid growth (as the inferred Eddington ratio is higher if $M_\bullet$ is lower (Rusakov et al. 2026)), thus revealing an evolutionary phase of intermediate mass and rapid growth that has remained elusive since the discovery of SMBH at high redshift (Fan et al. 2001; Inayoshi et al. 2020). On the other hand, for at least one object, the lensed LRD Abell2744-QSO1 (Furtak et al. 2024), there is a direct dynamical $M_\bullet$ measurement from spatially resolved ionised-gas kinematics. The inferred $M_\bullet$ for this object is substantially higher than what implied by the electron scattering model, indicating that the origin of the line broadening is not yet settled and warrants further investigation. It should also be noted that exponential Balmer-line wings are not unique to LRDs. Standard type-1 AGN are known to display a range of non-Gaussian broad-line profiles (e.g., Nagao et al. 2006; Kollatschny & Zetzl 2013), and a large subset of these AGN displays exponential wings (Trefoloni et al., in prep.), without sharing the other anomalies found in LRDs. In particular, reverberation mapping and even interferometric measurements support interpreting the heavy tails in these standard AGN as due to virial broadening, and in some cases to inner outflows (GRAVITY Collaboration 2018; GRAVITY+ Collaboration 2024, 2026), not radiative transfer effects. This suggests that a similar interpretation may apply to LRDs too. Motivated by this, a framework has been recently introduced to model the exponential wings of LRDs with emission from a stratified virialised BLR with no broadening from electron scattering (Scholtz et al. 2026; Madau et al. 2026).

Another key open question is the joint role of orientation and dust in LRDs: in the classical unified model of AGN, the inclination of a dusty, obscuring torus has an overwhelming impact on the observed SED (e.g., Urry & Padovani 1995). For LRDs, the hot dust component was initially found to be surprisingly faint compared to expectations (e.g., Setton et al. 2025a), although it is detected in several objects, with a luminosity that varies strongly from source to source (e.g., Juodžbalis et al. 2024; de Graaff et al. 2025) and correlates with the continuum spectral properties (Pérez-González et al. 2026). At the same time, distinctive features indicative of dense gas absorption are commonly detected in LRDs (e.g., Inayoshi & Maiolino 2025; de Graaff et al. 2025; D'Eugenio et al. 2026a). It remains debated whether the exceptional properties of LRDs require an entirely separate paradigm (e.g., Naidu et al. 2025) or instead at least some properties of the standard unification model can be applied also to LRDs (e.g., Madau & Maiolino 2026).

Progress on the LRD puzzle has been boosted by the discovery of local counterparts at $z \simeq 0.1$–0.2, which share the defining spectral features of high-redshift LRDs while permitting high signal-to-noise follow-up (Lin et al. 2026; Ji et al. 2026c). In particular, SDSS J102530.29+140207.3 ('The Egg' in Lin et al. 2026; 'Lord of LRDs' in Ji et al. 2026c; hereafter: J1025) exhibits broad Balmer lines, a 'v'-shaped spectral energy distribution (SED), deep Balmer-line absorption, forbidden [Fe II] emission (Lin et al. 2026; Ji et al. 2026c) and extreme X-ray weakness (Ji et al. 2026c). These nearby systems provide a unique laboratory to test existing theories of line broadening, dust obscuration and orientation effects in LRDs.

Polarimetry has historically been a decisive tool for mapping AGN structure and testing unification by orientation. Bypassing any obscuring medium, scattered light can effectively provide an additional, different sightline towards obscured systems. The spectropolarimetric detection of broad permitted lines in polarised flux in NGC 1068 provided direct evidence for a luminous, hidden BLR whose direct view is blocked by optically thick circumnuclear material, while scattered light escapes along less-obscured directions (Antonucci & Miller 1985). This result became a cornerstone of unified AGN models, in which type 1 and type 2 classifications largely reflect viewing angle relative to an obscuring torus and associated scattering regions (Antonucci 1993). Subsequent spectropolarimetric surveys demonstrated that a substantial fraction of Seyfert 2 galaxies harbour hidden BLRs, constraining both the ubiquity of obscuration and the geometry of the scattering medium (see e.g. Barth et al. 1999b,a; Moran et al. 2000; Tran 2003; Ramos Almeida et al. 2016 and references therein).

Within the standard unification model of AGN, polarimetry is a consolidated and powerful tool to probe the inner parsec in type-1 systems: the proximity of the polarising medium to the AGN means that polarised light can carry the imprint of spatially resolved information on physical scales that are impossible to resolve in total light. Optical spectropolarimetry of Seyfert 1 galaxies reveals diverse polarisation behaviours across broad lines and continua that can be understood in terms of competing equatorial and polar scattering components, with the observed polarisation degree and position angle strongly dependent on inclination (Smith et al. 2002, 2004; Goosmann & Gaskell 2007). Moreover, the wavelength-dependent polarisation angle and degree across the broad Balmer lines encode BLR kinematics and geometry, enabling complementary constraints on BLR structure (Smith et al. 2002, 2004) and even single-epoch black-hole mass measurements (Afanasiev & Popović 2015). Detailed equatorial-scattering models further show that large-amplitude blue-to-red swing in polarisation angle and wing peaks in polarisation fraction p arise naturally when a rotating line-emitting disc is surrounded by a compact coplanar scattering region (Smith et al. 2005).

At the same time, a polarised optical continuum does not necessarily imply a distinct external scattering region. Since the optical/UV continuum of AGN is widely attributed to accretion-disc emission, intrinsic continuum polarisation has long been expected from radiative transfer within the disc atmosphere, driven primarily by electron scattering. Plane-parallel electron-scattering calculations predict substantial polarisation at high inclination, although subsequent work showed that bound-free opacity, relativistic effects, non-planar disc geometries, and magnetic Faraday rotation can strongly alter both the degree and position angle of the emergent polarisation (Laor et al. 1990; Coleman & Shields 1990; Kartje & Königl 1991;

[1] Maiolino et al. (2024) reports that while LRDs exceed the local $M_\bullet$–$M_\star$ relation, they seem to lie on the local $M_\bullet$–σ relation, under the assumption that the measured velocity dispersion of the ionised gas σ is a faithful predictor for the velocity dispersion of the underlying stellar population (see also McClymont et al. 2026; Ortame et al. 2026). Reconciling the $M_\bullet$–$M_\star$ relation may therefore be in tension with the $M_\bullet$–σ relation.

Agol & Blaes 1996). A polarised AGN continuum therefore does not by itself require that the dominant polarisation arises in a separate external scattering medium, by which we mean material outside the continuum-emitting region, i.e. the accretion disc.

In this article we present optical linear spectropolarimetry of the local LRD J1025. After presenting the observations and data reduction (Section 2), we show the results of our analysis (Section 3) and discuss the implications (Section 4). We conclude with a summary of our findings in Section 5. Throughout this article, we assume the ΛCDM cosmology from the Planck Collaboration et al. (2020, their table 2). All wavelengths are air wavelengths, and line equivalent widths (EW) are in rest frame, with negative values corresponding to line emission. We adopt the standard IAU convention that the polarisation angle ϑ is measured from North to the East; we define the polarisation reference such that $(q, u) = (1, 0)$ and $(q, u) = (0, 1)$ denote polarisation along $\vartheta = 0°$ and $\vartheta = 45°$, respectively.

2 OBSERVATIONS AND DATA REDUCTION

We present optical linear spectropolarimetry of J1025 with VLT/FORS2 in PMOS mode, obtained by the dedicated ESO programme 115.29FY.001. The observations consisted of eight successful observing blocks (OBs), taken between UT 2025-12-23 and 2026-02-22. We rejected three additional OBs due to low signal-to-noise ratio (SNR) in one or more configurations. The on-chip seeing spanned a full-width at half maximum (FWHM) of 0.7–0.89 arcsec, as measured by fitting a Gaussian to the 2-d spectrum of the broad H α wings, which we assumed to be spatially unresolved (unlike narrow H α; Section 3.7). The PMOS setup used a 1-arcsec-wide slit and the GRIS 1200R grating, covering $5750 < \lambda < 7310$ Å at a resolution $R \simeq 2140$ at H α. This nominal resolution is consistent with the on-chip determination, where we find a $FWHM = 3.083$ Å at H α ($R = 2128$), obtained from fitting sky lines and interpolating linearly in wavelength to reach H α. We used the GG435 order-sorting filter and 2×2 on-chip binning to improve the SNR in the continuum and broad-line wings. Targeting linear polarisation, each OB was split into four retarder-plate position angles $\alpha = 0°, 22.5°, 45°$, and $67.5°$.

We reduced the data using the ESO Reflex standard pipeline for FORS2 spectropolarimetry, which performs bias subtraction, flat-field correction, wavelength calibration, sky subtraction, extraction of the ordinary and extraordinary beams, and derivation of Stokes $Q(\lambda)$ and $U(\lambda)$. The eight retained OB spectra were resampled onto a common wavelength grid and combined by computing the cross-OB median of $Q(\lambda)$, $U(\lambda)$, and $I(\lambda)$. We experimented with arithmetic means, clipped means, and inverse-variance weighting, but the median stack provided the cleanest suppression of residual artefacts while preserving the same qualitative line effects. Unless stated otherwise, all measurements refer to this median stack. We define the normalised Stokes parameters $q \equiv Q/I$ and $u \equiv U/I$, the fractional linear polarisation $p \equiv \sqrt{q^2 + u^2}$, and the quadrant-preserving polarisation angle $\vartheta \equiv 0.5 \arctan(u, q)$. The linearly polarised (hereafter simply 'polarised') flux is then the product $p \times I = \sqrt{U^2 + Q^2}$.

The stacked flux spectrum I is shown in Fig. 1; we used the SDSS Data Release 7 spectrum of the source (Abazajian et al. 2009) for absolute flux calibration. Our wavelength solution yields a redshift of $z = 0.100645$; after converting our FORS2 air wavelengths to vacuum to match SDSS, the residual offset from the SDSS redshift is -34 km s^{-1}. This is not due to our frame of reference, since both works use barycentric redshift, so we attribute this offset to systematics in our wavelength calibration. To avoid additional resampling, we adopt the FORS2 wavelength scale for the rest of this article. After correcting for this velocity shift, the FORS2 and SDSS spectra agree well across the full FORS2 range (Fig. 1), with the exception of the atmospheric B-band absorption near 6870 Å. We noticed a localised flux depression in the FORS2 data just blueward of H α (∼ 7200 Å observed), without a counterpart in SDSS; given the variability in both emission and absorption-line equivalent width tentatively reported in LRDs at $z = 5$–7 (D'Eugenio et al. 2026a; Ji et al. 2025; Furtak et al. 2025), but in light of the limited wavelength-calibration accuracy in this detector region, we simply note the feature but do not interpret it further.

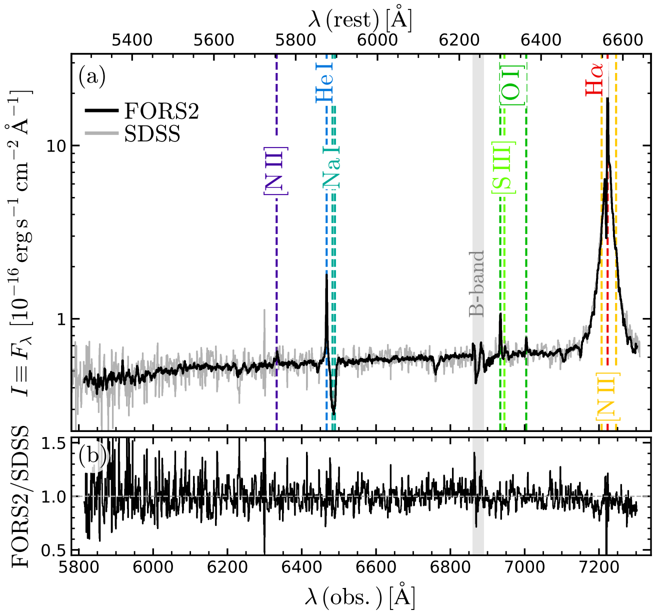

Figure 1. Flux-calibrated FORS2 spectrum of J1025 (black) compared with the archival SDSS spectrum (grey). The lower panel shows any residual flux-calibration mismatch. The grey shaded band marks the telluric B absorption band. The two spectra agree well across most of the wavelength range; a localised flux deficit in FORS2 relative to SDSS is visible just blueward of H α.

To validate our results, we inspected per-OB q–u profiles and polarised-flux spectra; we repeated our analysis by using a fixed box-car extraction (16 spatial pixels) instead of the default optimal extraction, and we used leave-one-out and leave-two-out stacking. For the latter test, removing any one OB does not affect our results; for example the changes in the median continuum or line polarisation are $\lesssim 0.2$ per cent (the largest change being 0.23 per cent).

The sightline towards J1025 is relatively free of Galactic dust, with $A_{V,\mathrm{MW}} = 0.14$ mag (Schlafly & Finkbeiner 2011; Ji et al. 2026c). Using the relation of Serkowski et al. (1975), this value implies an upper limit to the foreground (Milky-Way) polarisation of $p_{\mathrm{MW}} < 3 \times (A_{V,\mathrm{MW}}/\mathrm{mag})$ per cent, or 0.4 per cent. We additionally assessed the residual instrumental polarisation using nightly observations of unpolarised standard stars, finding $p_{\mathrm{inst}} \lesssim 0.2$ per cent. While non-negligible, these contributions are unlikely to account for the polarisation measured in our target (Section 4.1). In the remainder of the article, we do not subtract these contributions, but we discuss where they may be relevant and affect the interpretation of the data.

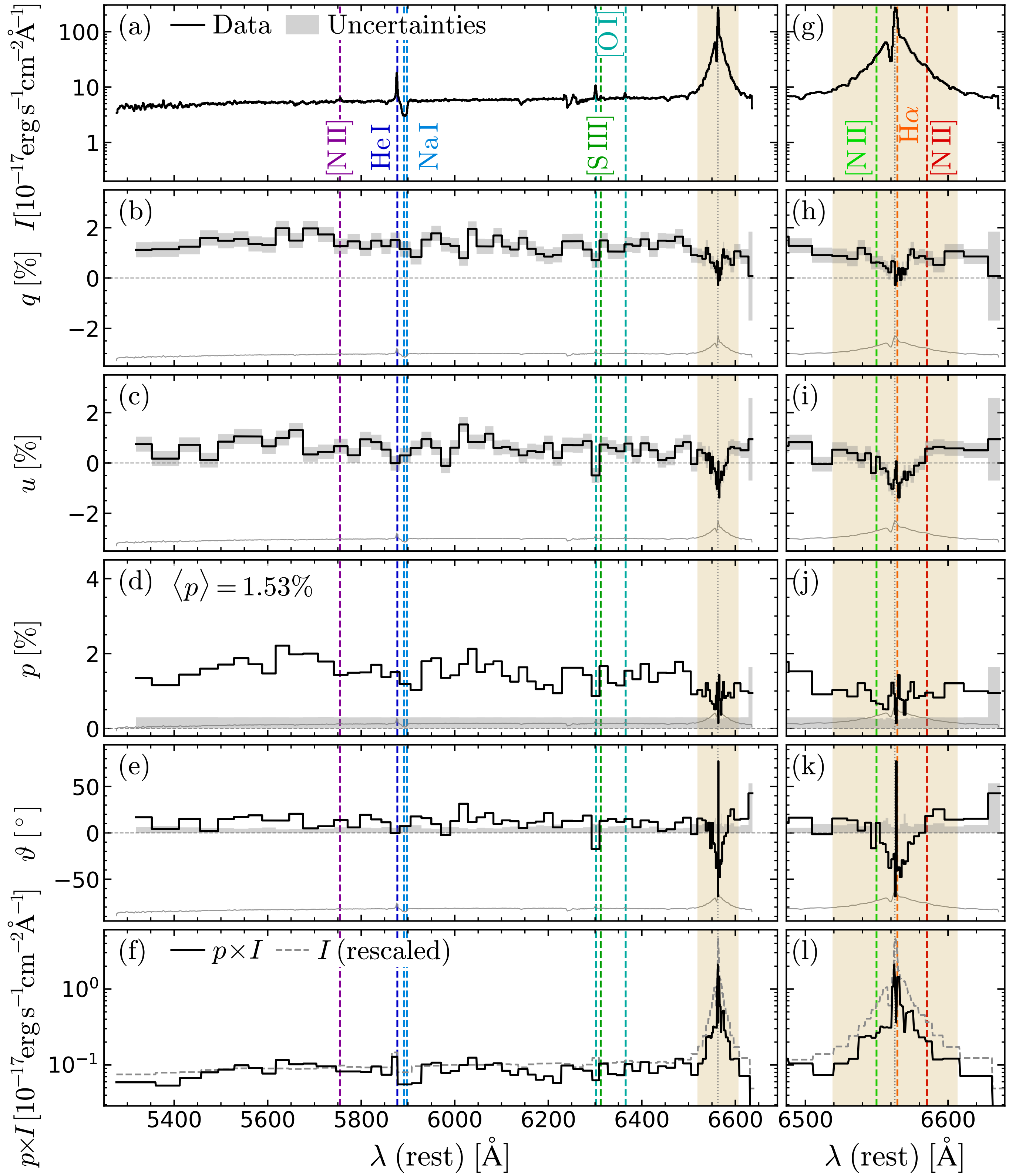

Figure 2. Optical linear spectropolarimetry of J1025 (binned adaptively to a fixed $\sigma(p) \simeq 0.3$ per cent, using the cross-OB median stack). The shaded vertical region encloses ± 2000 km s^{-1} from systemic H α. The continuum displays nearly grey polarisation, with $\langle p \rangle = 1.53 \pm 0.04$(rand.)$\pm 0.20$(syst.) per cent and a consistent $\vartheta = +12°$ over the available wavelength range (panel d), while broad H α is even less polarised (panel d and zoom-in panel j). We detect a swing in the polarisation angle between the continuum (near $\vartheta \simeq +12°$; panel e) and broad H α, which reaches $\vartheta \simeq -36°$, dipping locally to $\simeq -40°$ (panel k). The continuum polarisation is significantly detected and larger than any systematic effects such as foreground polarisation and residual instrumental effects (Section 2). The polarised flux $p \times I$ (panel f) follows the shape of total flux I (grey dashed line), whereas broad H α is clearly suppressed in polarised flux (panel l).

3 RESULTS

3.1 A polarised continuum

Fig. 2 summarises the optical spectropolarimetry data; the H α region is highlighted in sand colour (we show a zoom in the right panel). Stokes I is shown in the native binning, while all other panels are binned to overcome Rice bias in p (Wardle & Kronberg 1974) and periodic instabilities in the polarisation position angle ϑ. To preserve spectral resolution where the SNR allows it, we use an adaptive binning scheme, tailored to reach a target of 0.3 per cent noise in p.

The spectrum is clearly polarised (panel d), as also evident from the non-zero values of both q and u, ruling out any residual Rice bias after our adaptive binning (panels b and c). The polarisation value is fairly low, averaging $\langle p \rangle = 1.53 \pm 0.04$ per cent over the entire spectral window, after masking out H α, the weaker spectral features (He I λ5875, Na D, [O I]λλ6300,6364), and the telluric B band. This value is comparable to what found in many local Seyfert 1 galaxies (e.g., Smith et al. 2002, 2004; Afanasiev et al. 2019).

3.2 Grey polarisation curve

The spectral dependence of line polarisation carries information on the conditions of the source, and on the nature of the polarising medium. For example, electron scattering is wavelength independent (grey polarisation), while dust scattering is strongly wavelength dependent (e.g., Miller et al. 1991; Goosmann & Gaskell 2007). To test the wavelength dependence of p, we fitted local linear slopes to the continuum Stokes spectra over the full line-free continuum (Fig. 3), masking broad H α (±4000 km s^{-1}), He I λ5875 and Na D, the [O I]λλ6300,6364 doublet, and the telluric B band (rest-frame 6228–6264 Å). Once again, we must control for Rice bias, since the noise level increases at short wavelengths. We therefore derive $dp/d\lambda$ from the individual Stokes slopes. From the chain rule of $p \equiv \sqrt{q^2 + u^2}$ we obtain

$$\frac{dp}{d\lambda} = \frac{1}{p}\left(q\,\frac{dq}{d\lambda} + u\,\frac{du}{d\lambda}\right) . \quad (1)$$

We verified that this Stokes-space estimate is stable across all binning factors 1, 9, 16 and 25× (varying by $\lesssim$ 0.1 per cent per 1000 Å). In contrast, the direct slope fit from unbinned p is biased steep by a factor of 2.4, as expected from Rice bias disproportionately affecting blue wavelengths. We find only a weak decline in the continuum polarisation, with $dp/d\lambda = -0.26 \pm 0.15$ per cent per 1000 Å rest-frame (Fig. 3); all wavelength slopes quoted below are likewise given per rest-frame units. This result is driven by $dq/d\lambda = -0.19 \pm 0.15$ per cent per 1000 Å (panel a) and $du/d\lambda = -0.21 \pm 0.15$ per cent per 1000 Å (panel b), while considering that $q > 0$ and $u > 0$ over the whole wavelength range. A direct fit to the adaptively binned p spectrum gives a consistent result, $dp/d\lambda = -0.26 \pm 0.15$ per cent per 1000 Å. The signal of a spectral gradient in the polarisation of the continuum is therefore marginal in the median-stack analysis, hovering at $\simeq 1.7\,\sigma$ significance (the mean-stacked analysis returns a steeper, 3.5-σ slope, Appendix B).

Panel d shows the spectral slope of the polarised flux $p \times I$. For I, assuming $I(\lambda) \propto \lambda^{\beta}$, we measure $\beta = +1.6$ (in agreement with Ji et al. 2026c). For $p \times I$, we measure a slope steepening $\Delta\beta \equiv \beta_{p\times I} - \beta_I = -0.80 \pm 0.57$, i.e., the polarised continuum is statistically consistent with having the same spectral slope as the total flux, implying no significant evidence of wavelength dependence from the optical data alone. Clearly, a larger wavelength range is required to obtain a decisive proof of a polarisation gradient.

The mild redward slope in $p(\lambda)$ established above (Fig. 3) implies that the continuum polarisation declines at only $\simeq$ 0.3 per cent per 1000 Å, so the optical continuum is consistent with being approximately grey, at least over our limited ~1300-Å baseline in wavelength. We note that, because the empirical dichroic curve of Galactic dust is broad (shape parameter $K \simeq 1.15$; Serkowski et al. 1975) and our baseline is short, a dichroic $p(\lambda)$ peaking near our observed range would itself appear nearly grey, varying by $\lesssim$ 0.1 per cent across our baseline; our polarisation curve therefore does not discriminate against dichroic transmission.

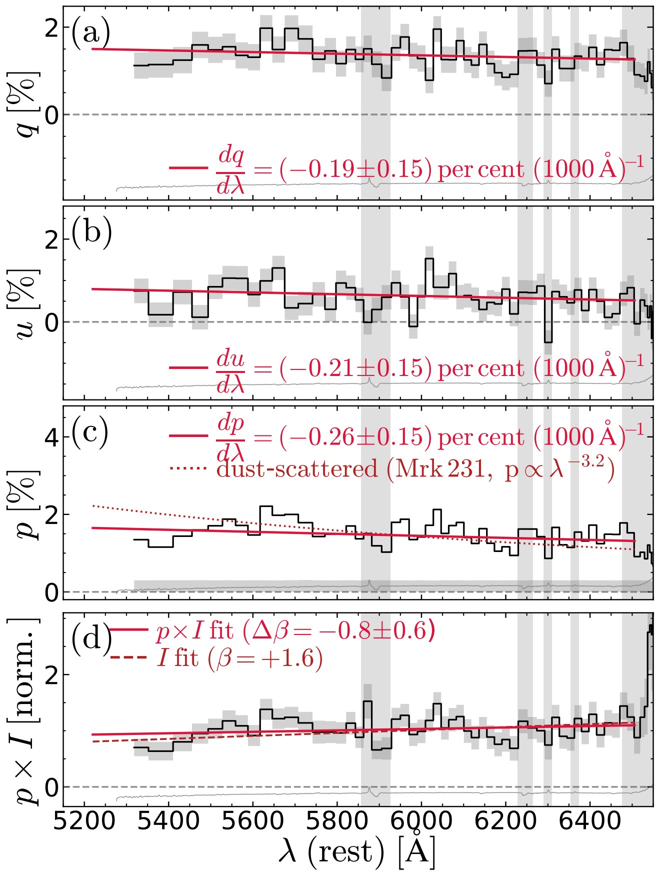

Figure 3. Continuum polarisation slope fit over the line-free continuum (the grey vertical bands are masked). In each panel, the black line and grey shaded band are the data and uncertainties, while the best-fit model is in red. Panels a and b show direct fits to q and u. Panel c shows the slope derived from combining the models for u and q, compared with the $p(\lambda)$ expected for Markarian-231-type dust scattering ($p \propto \lambda^{-3.2}$, dotted line; Smith et al. 1995), which is clearly inconsistent with the data. Panel d is a fit to the polarised flux (normalised at 5900 Å), reporting the slope difference $\Delta\beta$ with respect to the flux I, adopting the convention $F_\lambda \propto \lambda^{\beta}$; our data and the resulting best-fit model are consistent with grey scattering (dashed grey, the linear fit to I; electron scattering predicts $\Delta\beta = 0$).

3.3 Line polarisation

Across the brightest emission lines we detect line effects, i.e., localised changes in the polarisation degree p and/or position angle ϑ, confined to a line relative to the adjacent continuum (e.g., Antonucci & Miller 1985; Smith et al. 2002). Such effects are present at He I λ5875, [O I]λ6300, and both the broad and the narrow components of H α: in both q and especially u these lines deviate from the continuum (Fig. 2b and 2c). This is also visible as a depolarisation signal (localised drop in $p(\lambda)$) at the location of some of these lines,

Table 1. Polarisation and ancillary measurements of J1025. All per-wavelength units are rest-frame. Polarisation fractions are quoted as value ± statistical ± systematic, where the systematic is the instrumental polarisation $p_{\rm inst} \lesssim 0.2$ per cent (Section 2). The continuum-subtracted line quantities ($p_{\rm H\,\alpha}$, $\vartheta_{\rm H\,\alpha}$) are less sensitive to a constant Stokes-flux offset, but the exact line-only polarisation angle can still be shifted by a residual instrumental polarisation term because $p_{\rm H\,\alpha}$ is small (Section 3.4).

Quantity	Value
Continuum	
$p_{\rm cont}$	$1.53 \pm 0.04 \pm 0.20$ per cent
$\vartheta_{\rm cont}$	$+12 \pm 1°$
$dp/d\lambda$	-0.26 ± 0.15 per cent per $(1000\ \text{Å})^{-1}$
$\Delta\beta$	-0.8 ± 0.6
$p_{\rm cont}/A_{V,\rm MW}$	10.9 per cent mag^{-1}
Broad H α (cont. subtracted)	
$p_{\rm H\,\alpha}$	0.58–0.84 per cent
$\vartheta_{\rm H\,\alpha}$	$-34 \pm 3°$
$\Delta\vartheta = \vartheta_{\rm H\,\alpha} - \vartheta_{\rm cont}$	$-48 \pm 4°$

most notably [O I]λ6300 and H α. It is worth distinguishing two cases. Pure depolarisation by an intrinsically unpolarised line lowers p but preserves ϑ; a change in ϑ instead requires the line to carry its own polarisation at a different angle, and cannot arise from dilution alone. We see both: He Iλ5875, despite its higher equivalent width, keeps the continuum angle (consistent with simple dilution, and showing no significant u jump), whereas [O I]λ6300 shows a highly significant jump in u and a swing to negative ϑ, echoing broad H α (Fig. 2e).

Compared to the continuum, broad H α emission is significantly less polarised, with a central minimum near line peak reaching ≃0.5 per cent, approaching the ceiling of our systematic error (< 0.2 per cent). This drop in p is driven by both polarisation components: q tends to 0 for wavelengths approaching line centre, while u crosses 0 to reach opposite values with respect to the continuum average.

In principle, line depolarisation could be due to dilution of the polarised continuum by a completely depolarised emission line. Specifically, pure depolarisation would naturally explain the observed drop in q; it cannot, however, explain the change of sign in u, thus indicating that the H α line must have its own non-zero polarisation with a different angle with respect to the continuum. In mathematical terms, we can illustrate this with a simple model of flux-weighted mixing in Stokes space. If the continuum and line have Stokes parameters $(q_{\rm c}, u_{\rm c})$ and $(q_{\rm H\,\alpha}, u_{\rm H\,\alpha})$, then

$$q_{\rm obs} = \frac{q_{\rm c}F_{\rm c} + q_{\rm H\,\alpha}F_{\rm H\,\alpha}}{F_{\rm c} + F_{\rm H\,\alpha}}, \quad u_{\rm obs} = \frac{u_{\rm c}F_{\rm c} + u_{\rm H\,\alpha}F_{\rm H\,\alpha}}{F_{\rm c} + F_{\rm H\,\alpha}}, \tag{2}$$

Therefore, the observed drop in polarisation across H α cannot be fully explained by flux dilution due to an unpolarised line, but must be sustained by low-level polarisation of the line itself.

We also rule out that the drop in p across H α can be explained by a smooth continuum trend, since q clearly rises again after the line trough (Fig. 2i), and u even rises to the same magnitude as blueward of H α.

Confirming the hypothesis of a non-zero position-angle offset ($\Delta\vartheta \neq 0$ above), we detect a change in polarisation angle between the constant value seen in the continuum, $\vartheta_{\rm cont} \simeq +12°$, and H α. The wavelength trends in both u and q show that the change is genuine, although the actual angle is strongly diluted by the continuum Stokes vector (see Section 3.4 for the continuum-subtracted angle).

Non-null line polarisation is also evident in the q–u plane (Fig. 4). The blue-tail points are offset towards the origin, consistent with both lower polarisation and dilution, but H α shows a clear centroid offset from the continuum direction, confirming the offset in polarisation angle and ruling out pure dilution. There is also a clearly visible increase in scatter relative to the continuum points, despite the measurement uncertainties being the same, due to the adaptive binning. Note that the points do not form a rotation-driven loop, but are instead consistent with a weak additional Stokes component in the line, while the scatter may be indicating a more structured or multi-component H α-forming region (e.g., Ji et al. 2026a). Taken together, the total line spectropolarimetry shows that both the continuum and broad H α are polarised; while less polarised than the continuum, the polarisation of the broad line cannot be explained solely by continuum dilution due to an unpolarised line, so a weak intrinsic broad-line Stokes component is required.

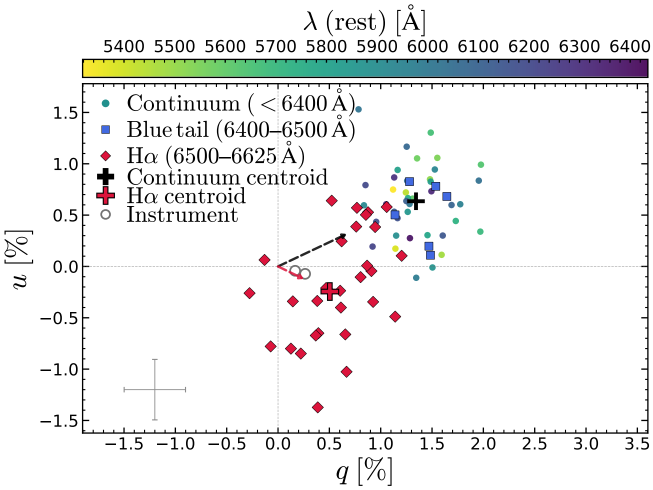

Figure 4. q–u plane diagram for the adaptively binned stacked spectrum. Small dots, coloured by rest-frame wavelength, show the continuum (λ < 6400 Å; bins falling in the telluric B band and on the [O I]λλ6300,6364 doublet are excluded). Larger markers highlight the blue-tail (6400– 6500 Å) and H α (6500–6625 Å) windows. The black and red crosses mark the continuum and H α centroids (inverse-variance-weighted means). The grey empty circles show the instrument polarisation, which we do not remove. H α shows a modest centroid offset and increased scatter relative to the continuum locus. This supports the presence of a weaker but non-zero Stokes component in the line.

3.4 Continuum-subtracted H α polarisation

The H α line has a lower polarisation fraction than the continuum ($p_{\rm H\,\alpha} < p_{\rm c}$), but the absolute polarised flux is still enhanced at H α: Fig. 2f shows that near the location of the H α peak, $p \times I$ is ∼ 4 times higher than the continuum polarised flux. Of course, this is due to the line's large total flux, which amplifies even a small polarisation fraction. To quantify the intrinsic polarised line signal more directly, we subtract a constant continuum Stokes component, measured as the mean of the adaptively binned Stokes-flux spectra I, $Q = qI$, and $U = uI$ over 6200–6400 Å (with the same masks as Section 3.1). All line-only quantities below derive from the resulting binned, continuum-subtracted Stokes fluxes. The residual line-only Stokes profiles (Fig. 5b) show a coherent signal: $Q_{\rm H\,\alpha}$ is systematically positive across the entire profile, whereas $U_{\rm H\,\alpha}$ is mostly negative, but with a narrow positive spike at the line core. We then condense these profiles into two moments over the H α window (6500–6625 Å; Fig. 4), which contains almost the entirety of the line flux: the wavelength-integrated polarisation, i.e., the coherent modulus of the summed Stokes fluxes, and the wavelength-average polarisation, i.e., the median of the per-bin p (Table 1). The first yields $p_{\mathrm{H}\,\alpha} = 0.58 \pm 0.24$ per cent, the second $p_{\mathrm{H}\,\alpha} = 0.84$ per cent (larger because the per-bin moduli are defined positive and blind to the angle oscillations leading to partial vector cancellation in the coherent sum). Hence we use $p_{\mathrm{H}\,\alpha} = 0.58$–$0.84$ per cent as the fiducial range. From bootstrapping, we obtain a 95$^{\mathrm{th}}$-percentile upper bound of $p_{\mathrm{H}\,\alpha} < 0.96$ per cent, lower than the continuum average $p_{\mathrm{c}} = 1.53$ per cent.

Moving to the polarisation angle, the same continuum-subtracted Stokes fluxes (Fig. 5) yield a line-integrated angle $\vartheta_{\mathrm{H}\,\alpha} = -34 \pm 3°$, offset by $\Delta\vartheta \equiv \vartheta_{\mathrm{H}\,\alpha} - \vartheta_{\mathrm{cont}} \simeq -48°$ from the continuum vector based on the same procedure ($\vartheta_{\mathrm{cont}} \simeq +14°$ in the masked sideband; the full-range continuum angle is $+12 \pm 1°$, Table 1). We detected no blue-to-red swing in the line.

As a foreground check, we repeated the same Stokes-space measurement after subtracting a constant Galactic Stokes vector with amplitude fixed either to a typical value, $p_{\mathrm{MW}} = 0.2$ per cent, or to the maximum allowed by the sightline, $p_{\mathrm{MW}} = 0.4$ per cent, while allowing its position angle to take any value. The offset changes for some foreground angles but is not removed: the minimum absolute offset is $\simeq 39°$ for $p_{\mathrm{MW}} = 0.2$ per cent and $\simeq 31°$ for $p_{\mathrm{MW}} = 0.4$ per cent. A residual instrumental polarisation at the level indicated by the zero-polarisation standards, $p_{\mathrm{inst}} \simeq 0.2$–$0.3$ per cent, is formally equivalent to the foreground test and we can therefore conclude that the angular shift between line and continuum is robust also with respect to instrumental polarisation.

We warn that even in the adaptively binned data, both ϑ and p display strong fluctuations near line centre. These could be due either to the fact that p is small in this region, so ϑ is correspondingly less stable, and/or to the McLean effect (McLean 1979; Ababakr et al. 2017), in which absorption near line core preferentially removes direct, unpolarised light, leaving the trough relatively enriched in scattered (and hence polarised) photons, thus raising the local polarisation.

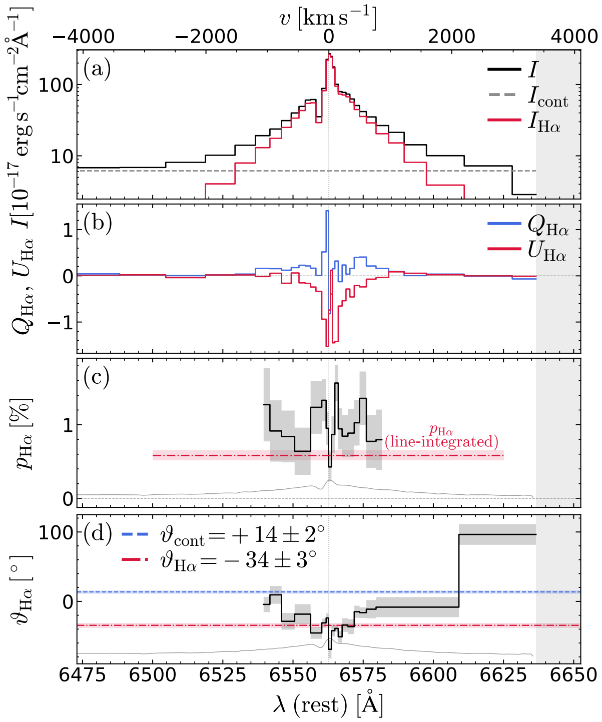

Figure 5. Continuum-subtracted Stokes-angle for broad H α in the adaptive-binned median stack. We subtract the constant continuum Stokes vector (the mean of the binned Stokes-flux spectra $\boldsymbol{I}$, $\boldsymbol{Q} = q\boldsymbol{I}$, and $\boldsymbol{U} = u\boldsymbol{I}$ over 6200–6400 Å), before recomputing $p_{\mathrm{H}\,\alpha}$ and $\vartheta_{\mathrm{H}\,\alpha}$. The top panels show the continuum and residual line-only Stokes fluxes. Panel c shows the continuum-subtracted $p_{\mathrm{H}\,\alpha}(\lambda)$; the dash-dotted line and band mark the 'coherent' (line-integrated) polarisation, $p_{\mathrm{H}\,\alpha} = 0.58 \pm 0.24$ per cent; note the per-bin values are positive-definite moduli, insensitive to the angle rotation, so they lie systematically above the line-integrated value (Section 3.4). Panel d shows the continuum-subtracted position angle. A robust line angle offset is present, without a blue-to-red swing in $\vartheta_{\mathrm{H}\,\alpha}$. The grey shading are beyond the spectral coverage.

3.5 Constraints from the polarised-flux spectrum

To test whether the polarised-flux line profile is broader than the total-flux profile, as often seen in AGN lines subject to scattering by an external medium (e.g., Smith et al. 2005; Goodrich & Miller 1994), we also fit the adaptively binned $p \times I$ spectrum with a linear continuum plus narrow and broad Gaussian H α components (Fig. 6). This fit yields $FWHM_{\mathrm{broad}}(p \times I) = 1740 \pm 400\ \mathrm{km\,s^{-1}}$ and $FWHM_{\mathrm{narrow}}(p \times I) = 214 \pm 43\ \mathrm{km\,s^{-1}}$. These are the widths of the two Gaussians fitted to the polarised flux, and should not be confused with the observed broad-line width in total light ($FWHM_{\mathrm{obs}} = 934 \pm 10\ \mathrm{km\,s^{-1}}$; Ji et al. 2026c) or the intrinsic, deconvolved width in the electron-scattering model ($FWHM_{\mathrm{int}} = 500 \pm 28\ \mathrm{km\,s^{-1}}$; Section 3.6).

The broad polarised component is consistent with the broadest Gaussian of the two-component direct fit ($FWHM \simeq 2000\ \mathrm{km\,s^{-1}}$; Burke et al. 2021; Ji et al. 2026c) and larger than the single-Gaussian total-intensity broad line. Given the large uncertainties, however, it is consistent within 1–3σ with essentially the entire range of total-intensity broad-line widths, from the $\simeq 500\ \mathrm{km\,s^{-1}}$ intrinsic model value to the $\simeq 2000\ \mathrm{km\,s^{-1}}$ broad Gaussian. Crucially, we do not find the markedly broader polarised line seen in some scattered-line AGN, where a narrow direct core coexists with much broader scattered wings (e.g., Miller et al. 1991; Goodrich & Miller 1994; Laor 2006): as Fig. 6 (bottom) shows, the continuum-subtracted $p \times I$ and I profiles, normalised to the same integrated area and binning, are mutually consistent.

To measure the exponential wing width of the polarised flux, we fit $p \times I$ with a linear continuum, a narrow Gaussian (the narrow polarised component above), and an exponential; the continuum is anchored to the line-free windows, where it is well determined. The fit yields $W_{p \times I} = 490 \pm 130\ \mathrm{km\,s^{-1}}$, which is statistically consistent with the exponential width of the total-flux fit, $W_I = 550 \pm 10\ \mathrm{km\,s^{-1}}$ (Section 3.6).

The narrow polarised component ($214 \pm 43\ \mathrm{km\,s^{-1}}$) is, in turn, much broader than the genuine narrow H α line ($\sigma \simeq 27$–$40\ \mathrm{km\,s^{-1}}$; Ji et al. 2026c; Lin et al. 2026), which presumably traces the host galaxy (marginally resolved at a physical scale of ~ 0.5 kpc, Section 3.7) and appears in polarised flux as a depolarisation dip, so it does not set the polarised width. The $214 \pm 43\ \mathrm{km\,s^{-1}}$ component is therefore incompatible with the host narrow line.

3.6 Illustrative mixed direct-plus-scattered H α fit

The addition of polarimetric data to the spectrum motivates a phenomenological test in which the observed profile is built from a dominant direct broad-line core plus a weaker, broader electron-scattered component. For Stokes-I we use the same model as Rusakov et al. (2026, as implemented in D'Eugenio et al. 2025; Ji et al. 2026c), consisting of a linear continuum, a direct broad H α component, and a broader scattered component with exponential wings. We also add

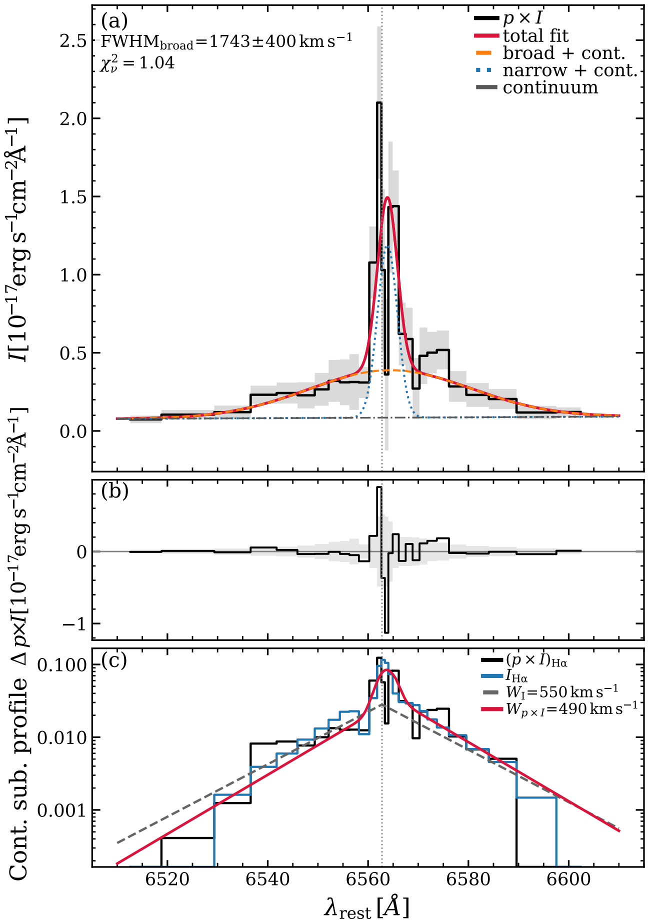

Figure 6. Fit to the adaptive-binned polarised-flux spectrum $p \times I$ around H α. Panel a shows the linear continuum plus narrow and broad Gaussian decomposition, yielding $FWHM_{\rm broad}(p \times I) = 1740 \pm 400$ km s^{-1} and $FWHM_{\rm narrow}(p \times I) = 214 \pm 43$ km s^{-1}. Panel b shows the residuals. Panel c compares the continuum-subtracted $p \times I$ to the (rescaled) I: the two profiles overlap along the entire line. The solid red curve is the double-Gaussian $p \times I$ model, while the dashed grey curve overplots an exponential with $W = 550$ km s^{-1}, as per our toy-model fit in total light (Section 3.6). The two wing widths are statistically consistent with each other, but the uncertainties on $W_{p\times I}$ are large (see text).

a narrow-line complex and an absorbing component near line centre, which we model using the optical depth model (e.g., Rupke et al. 2005; see D'Eugenio et al. 2026a,b for applications in the context of LRDs). For p, we assume that the continuum is polarised with $p_{\rm cont}$ = 1.51 per cent (Section 3.1), the direct broad and narrow lines are completely unpolarised, while the broad-scattered line is polarised with free $p_{\rm H\alpha}$. The model is then optimised against both the flux I and p, in a narrow range within −4000–3000 km s^{-1} from line centre.

The resulting flux model is shown in Fig. 7a, and the best-fit parameters are listed in Table 2, alongside the measurement uncertainties. We believe that the true uncertainties are dominated by systematic errors due to the limitations of the model, hence some of the formal values in the table may be underestimated. The extent of systematics can be gauged by inspecting the fit residuals (Fig. 7b), where high-significance undulations point to substantial data–model mismatch. This discrepancy may point to unaccounted for absorption and/or weak emission, and to a breakdown of some of the other assumptions, such as the fact that the narrow lines and absorption line are themselves unpolarised. However, delving into the absorption-line characterisation of LRDs is still challenging (e.g., Ji et al. 2026c), and is thus beyond the scope of the toy model and, first and foremost, of this paper too. With these limitations in mind, the best-fit parameters are in good agreement with the results of Ji et al. (2026c), who based their analysis on twice-higher resolution spectroscopy from Gemini GMOS (Burke et al. 2021). Specifically, we find $\tau_{\rm e}$ = 1.58 ± 0.07 against 1.79 ± 0.05, our exponential kernel has width W = 554 ± 12 km s^{-1}, while their value is 569 ± 4 km s^{-1}, and the intrinsic BLR has $FWHM$ = 500 ± 28 km s^{-1}, very close to Ji et al. (2026c)'s 520 ± 10 km s^{-1}. Interestingly, we note that the narrow-line width $\sigma_{\rm n}$ = 10 ± 5 km s^{-1} is remarkably smaller than in Ji et al. (2026c), and more in line with the value of ≃ 27 km s^{-1} from Lin et al. (2026), who used higher resolution still. Among these model parameters, $\tau_{\rm e}$ provides independent constraints on the amount of scattering underwent by H α photons, which is crucial to break the degeneracy between polarised fraction and geometry.

Table 2. Best-fit parameters for the toy electron-scattering spectral model (see Fig. 7).

Label	Value±Err	Units
$z_{\rm n}$	0.100649 ± 0.000003	[—]
$\sigma_{\rm n}$	10 ± 4	[km s^{-1}]
$F_{\rm n}$(Hα)	910 ± 20	[10^{-17} erg s^{-1} cm^{-2}]
$F_{\rm n}$([N II]λ6583)	13 ± 2	[10^{-17} erg s^{-1} cm^{-2}]
$FWHM_{\rm BLR}$	500 ± 30	[km s^{-1}]
$F_{\rm b}$(Hα)	2670 ± 40	[10^{-17} erg s^{-1} cm^{-2}]
$\tau_{\rm BLR}$	1.58 ± 0.07	[—]
W	550 ± 10	[km s^{-1}]
$v_{\rm abs}$	−50 ± 2	[km s^{-1}]
$\sigma_{\rm abs}$	74 ± 5	[km s^{-1}]
$\tau_{0,\rm H\alpha}$	3.2 ± 0.6	[—]
C_f	1.00 ± 0.07	[—]
$p_{\rm broad}$	0.8 ± 0.5	[%]

Fig. 7c shows that this simple model reproduces the two key qualitative properties of the data at the same time: depolarisation in the line core and a recovery of the polarisation fraction toward the wings, where the model reaches the continuum value. Note that the polarisation reaches ≃ 0 at line centre due to the contribution of the unpolarised narrow component of H α. We note that the fit is not statistically acceptable, and the parameters are strongly degenerate, so we do not regard it as a quantitative inference tool. In particular, the model strongly underpredicts p close to the line core, pointing to complex behaviour near line resonance (e.g., Chang et al. 2026), clumpy structure (e.g., Ji et al. 2026a), or hard-to-model contribution from the host galaxy (e.g., Torralba et al. 2026; Matthee et al. 2026). However, we also stress that the model–data mismatch is not driven by the polarised fraction alone: as discussed previously, significant shortcomings are also present in the flux model itself, and these are not driven by the simultaneous fit to p, since they persist with nearly identical shape and statistical significance when fitting Stokes I alone (cf. Fig. 7b and Fig. C1 from Appendix C). In summary, this model provides a useful proof of concept for assessing the plausibility of some electron-scattered contribution to the broad-line wings. Finally, a double-Gaussian parametrization of the broad line would also reproduce the data (e.g., Ji et al. 2026c).

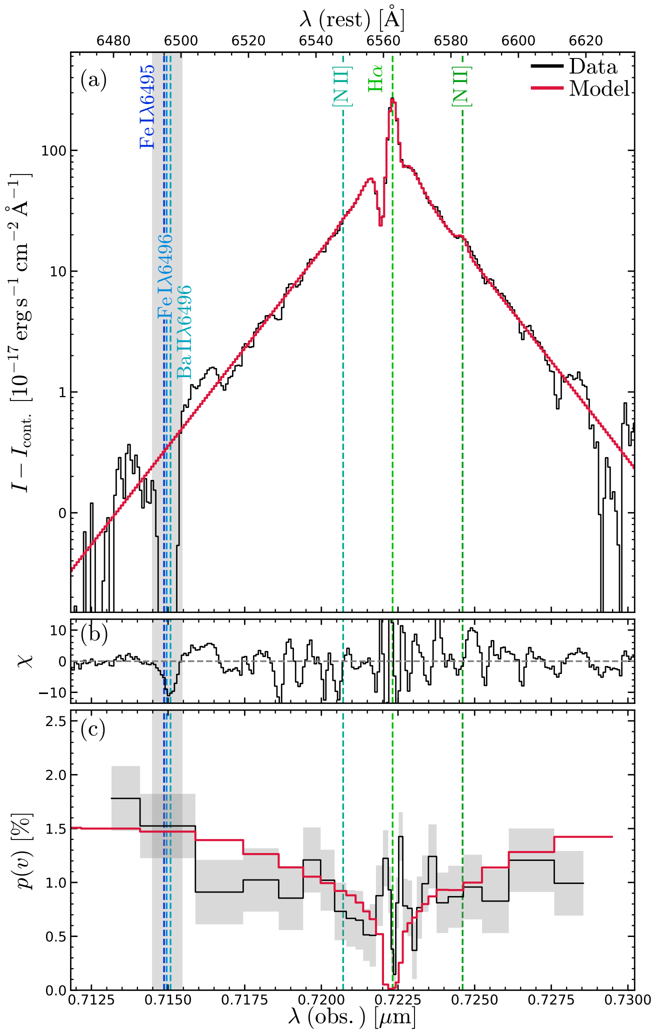

Figure 7. Illustrative toy model for a mixed direct-plus-scattered H α profile. Panel (a) compares the native-resolution median-stack total-flux spectrum (continuum-subtracted; black) with the best-fitting I-only model (red). Panel (b) shows the corresponding residuals. Panel (c) shows the resulting polarisation fraction p across H α (model, red; data, black), which reproduces the core depolarisation and the recovery of p towards the continuum value in the wings. The model contains a direct broad H α component, a broader electron-scattered component with approximately exponential wings, a narrow-line complex, and an absorbing component near line centre. Although the model correctly reproduces the overall trend of I and p, significant residuals remain in both quantities, most notably close to the core of the line, indicative of an inherent complexity of the line forming region(s) for this object.

3.7 Spatially resolved narrow H α

In Fig. 8 we compare the spatial profile of the narrow and broad H α line as measured in three OBs, ordered top to bottom by increasing image quality. The left column (panels a, c and e) shows the empirical comparison, illustrating that in all OBs, narrow H α (black) is more extended than both the blue and red wing of broad H α (blue and red curves, obtained as the average flux density within rest-frame 6550–6556 Å and 6572–6578 Å). The bottom panels show the ratio between narrow H α and the broad-H α wings. The strong and systematic departure from unity (horizontal dashed line) implies that narrow H α is more extended. Furthermore, the consistent behaviour of the blue and red curves highlights the stable PSF shape between the blue and red wings of broad H α, as expected given the short wavelength separation. Crucially, evidence of spatial extension increases with improving image quality.

In the right column we quantify the spatial extension of H α, adopting as instrument PSF the average between the spatial profiles of the blue and red broad-H α wings (grey dashed line). We model the spatial profile of narrow H α as an exponential, with half-light radius $R_{\rm e}$. We then convolve this exponential with the PSF (which already accounts for slit convolution) to match the data. The best-fit model is shown by the green curve, while the bottom panels display the fit residuals. From the best-seeing OB (OB03) we infer $R_{\rm e} = 0.23 \pm 0.01$ arcsec, corresponding to 440 ± 19 pc at $z = 0.1006$. This value is comparable to the *HST*-based $R_{\rm e}$ for the local LRD J1047 ($R_{\rm e} = 500$ pc; Lin et al. 2026), and to the narrow-line sizes inferred in a lensed LRD at $z = 7.04$ (Juodžbalis et al. 2026b). Nevertheless, we also notice systematic negative residuals near the profile core, indicating that the adopted model function may not fully capture the galaxy profile. Since the residuals are mostly negative in the centre and positive at large radii, we speculate that a Sérsic index $n > 1$ may be preferred over our assumed exponential.

We note that the fit residuals are structured across all three OBs, with the fiducial exponential model typically over-predicting the flux near the core ($\lesssim 1$ arcsec). To test if this reflects the adopted PSF or the source model, we explored several variations of the model fit. Replacing the empirical broad-line PSF with a Moffat fit improves the fit only modestly ($\chi^2 = 14.4$ instead of 19.2), while symmetrising the empirical PSF alone does not help. In contrast, replacing the exponential source profile with a Sérsic model substantially improves the fit ($\chi^2 = 7.7$ with the empirical PSF, and 5.9 with the Moffat PSF), but the inferred Sérsic indices are $n \simeq 4.5$ and $n \simeq 3.1$, uncharacteristically large for a gas distribution. Nevertheless, these fits suggest that the dominant mismatch is due to the adopted source profile rather than to the PSF model. If both the narrow-line profile and the PSF are symmetrised about their centroids, an exponential model yields a remarkably smaller $\chi^2 = 0.4$. In this case, $R_{\rm e} \simeq 0.08$ arcsec, but this approach is very risky, because the source is only marginally resolved; hence it is hard to assess if the symmetrisation procedure biases the inferred radius.

4 DISCUSSION

Our spectropolarimetry yields a small number of largely model-independent results, which we then use to address a sequence of physical questions. The results are:

(i) the continuum is polarised at $p_{\rm cont} \simeq 1.5$ per cent, while broad H α is less polarised ($p_{\rm H\,\alpha} = 0.58$–0.84 per cent; Section 3.4) with an offset in the line polarisation angle of $\Delta\vartheta \simeq -48°$;
(ii) the continuum polarisation is nearly grey;
(iii) we detect no blue-to-red swing in polarisation angle across the line;
(iv) the width W of the exponential model is statistically consistent between polarised and total light (within our large uncertainties);
(v) narrow H α is spatially more extended than the broad-line wings.

The discussion is organised around the physical questions these results help to address. After establishing that the signal is intrinsic and not foreground (Section 4.1), we summarise which mechanisms can polarise the source. Given the debated nature of LRDs, we adopt a physics-first approach: we derive our constraints from the data and from general physical arguments, to avoid biasing the interpretation

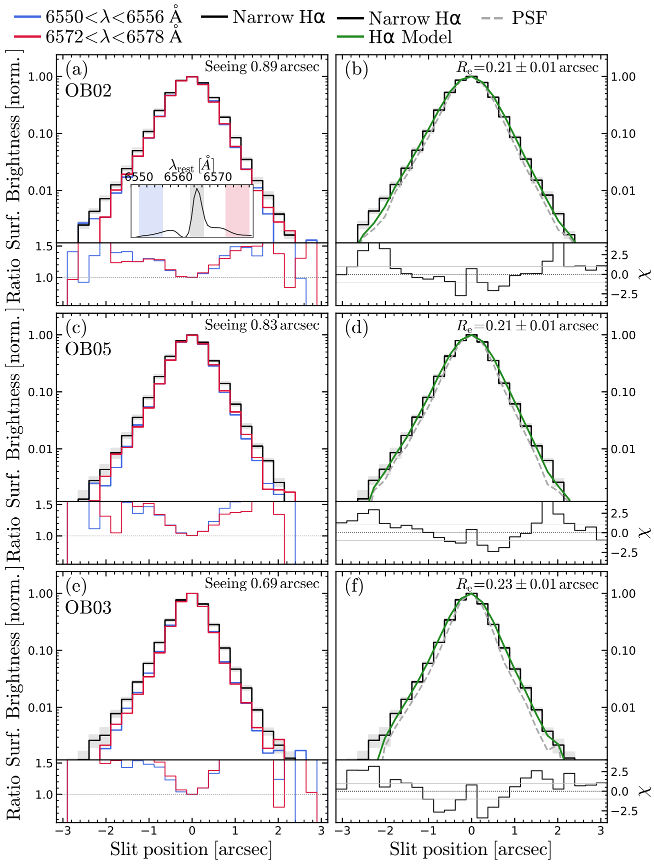

Figure 8. Spatial profile comparison between narrow H α (black) and broad H α, which we use as a point-source reference. Each row shows a different OB, ordered by increasing image quality. The left column (panels a, c and e) shows the data, normalised to the peak flux density, with the blue and red wings of broad H α in blue and red, respectively (the inset in panel a displays the three spectral windows we averaged to obtain the narrow and broad-line profiles). The bottom panels show the narrow-to-broad ratio, with increasingly strong departures from unity as image quality improves. The right column (panels b, d and f) shows the best-fit exponential model of narrow H α (green), convolved with the PSF (dashed grey), taken to be the average of the red and blue broad-line wings of H α. The bottom panels show the χ residuals, with systematic departures suggesting a structured narrow-line profile or deviations from a simple exponential model. The inferred R_e is reported in the top right corner.

towards familiar source classes. We thus discuss the continuum (Section 4.3), continuum–line differences (Section 4.4), and the broad H α line (Section 4.5). We defer the comparison with the extensive AGN-polarisation literature to Section 4.7. Finally, Section 4.8 provides our preferred interpretation.

4.1 The polarisation is intrinsic to J1025

A purely Galactic foreground dust screen cannot explain the observed spectropolarimetry. Such a screen would impose the same wavelength-dependent Stokes vector on both continuum and line photons, while the data show a localised line effect across broad H α.

At the high Galactic latitude of J1025 ($b \simeq +54°$), Galactic foreground dust is minimal: we find $A_{V,\mathrm{MW}} = 0.14$ mag (from both Schlafly & Finkbeiner 2011 and *Planck*, Planck Collaboration 2015; we converted $E(B-V)$ measurements to $A_{V,\mathrm{MW}}$ assuming the Cardelli et al. 1989 law with $R_V = 3.1$). For such low dust columns, the *Planck* 353-GHz polarised-dust maps are noise dominated (Planck Collaboration 2015, 2020), so the foreground polarisation angle is unconstrained. Nevertheless, even assuming the maximum interstellar polarisation efficiency (i.e., the empirical Serkowski et al. 1975 ceiling $p/A_{V,\mathrm{MW}} \leq 3$ per cent mag^{-1}, reached only for ideally aligned grains with the magnetic field in the plane of the sky, Andersson et al. 2015), the Galactic foreground along this sightline would be $p_{\mathrm{MW}} < 0.4$ per cent, below both p_{cont} and $p_{\mathrm{H}\alpha}$. Assuming typical efficiencies (2–3 times below the ceiling; e.g., Fosalba et al. 2002), the realistic Galactic polarisation is $p_{\mathrm{MW}} < 0.2$ per cent and thus sub-dominant in our observed signal. Turning the argument around, if the observed continuum signal were dominated by Galactic extinction, it would require $p_{\mathrm{cont}}/A_{V,\mathrm{MW}} \simeq 10.9$ per cent mag^{-1}, several times higher than the maximum efficiency.

We conclude that while Galactic foreground polarisation may still contribute at a sub-dominant level, it cannot dominate the observed signal. Given our inability to accurately measure the foreground polarisation, we quote only the amplitude limit $p_{\mathrm{MW}} < 0.4$ per cent and do not attempt a Stokes-space foreground subtraction.

The line effect is the key point: even if the foreground contribution were larger than expected for this particular sightline, a smooth foreground screen cannot produce the observed change in polarisation fraction and polarisation angle across the broad line. The polarisation signal must therefore be primarily intrinsic to J1025.

4.2 Polarisation mechanisms and their signatures

Before addressing what polarises the continuum and the broad line, it is useful to review the relevant polarisation mechanisms and their distinguishing signatures. Polarisation can be (i) intrinsic, i.e. generated within the atmosphere of the source itself, through radiation transfer in a scattering-dominated, aspherical, highly ionised atmosphere (in AGN, the accretion-disc atmosphere; Laor et al. 1990; Coleman & Shields 1990; Kartje & Königl 1991; Afanasiev et al. 2019); or extrinsic, driven by (ii) electron scattering in ionised gas outside the source, (iii) dichroic transmission through magnetically aligned dust grains, or (iv) dust scattering. The polarisation amplitudes are set by different quantities.

Intrinsic polarisation is set by the optical depth of the source, by the asphericity of the emitting medium, and by its inclination to the line of sight, reaching, in the optically thick limit, a theoretical maximum of 11.7 per cent for a pure electron-scattering atmosphere viewed edge-on, and decreasing monotonically to $p = 0$ with decreasing inclination i (Chandrasekhar 1960). Externally scattered light can be polarised at tens of per cent, depending on the scattering angle. Dichroic polarisation is set by the dust column, grain composition, and degree of grain alignment: NIR polarimetry of Seyfert-2 nuclei implies that AGN-local dust is generally inefficient, $dp/dA_V \sim 0.1$–0.3 per cent mag^{-1} (e.g., Young et al. 1995; Lumsden et al. 1999), well below the maximum Galactic value (∼ 3 per cent mag^{-1}, measured at optical wavelengths; Serkowski et al. 1975).

These mechanisms also differ in their wavelength dependence. Electron scattering, whether in the source atmosphere or in external ionised gas, produces grey polarisation. For intrinsic polarisation, deviations from a grey curve can arise from a number of radiative transfer effects (Laor et al. 1990; Coleman & Shields 1990; Agol & Blaes 1996; Gnedin et al. 2005; Afanasiev et al. 2019), which together predict a non-monotonic wavelength dependence. Uniquely among these mechanisms, electron scattering, when it acts on emission lines and has sufficient optical depth, also produces substantial broadening (e.g., Laor 2006; Chang et al. 2026, which we discuss in Section 4.6). Dichroic polarisation peaks near optical wavelengths for Milky-Way-like grains ($\lambda_{\max} \simeq 0.55$ μm; Serkowski et al. 1975), shifting with the size of the aligned grains (Whittet et al. 1992), which in AGN may differ from Galactic dust (e.g., Maiolino et al. 2001); the cross section for dust scattering, instead, rises towards the blue (cf. the dust- and electron-scattered sightlines in NGC 1068; Miller et al. 1991). Our nearly grey polarisation curve (Fig. 3) is consistent with electron scattering, but our short optical baseline cannot single out a unique mechanism from the polarisation curve alone (Appendix B).

4.3 The optical continuum

4.3.1 A single dominant source

Most LRD models assume a single, dominant source for the optical continuum, be it a massive accreting black hole (e.g., Madau & Maiolino 2026; Rusakov et al. 2026) or a supermassive star (e.g., Nandal & Loeb 2026). Here we ask if the data support this assumption.

While our observations partially resolve the host galaxy (or an extended narrow-line region, $R_e = 440 \pm 19$ pc; Section 3.7), host-galaxy light cannot explain the continuum in J1025, as standard stellar populations are known not to reproduce its observed spectral features (Lin et al. 2026). Our continuum polarisation also rules out a population of non-standard, emission-line stars. Many distinct and comparable sources would not naturally combine into one coherent continuum Stokes vector, yielding small net polarisation. N comparable sources with polarisation p^* and random polarisation orientations yield an average net polarisation $\approx p^*/\sqrt{N}$; therefore, explaining $p_{\rm cont}$ with N sources requires $p^* \gtrsim p_{\rm cont}\sqrt{N}$; comparing the H α luminosity of J1025 to that of the most luminous emission-line star (NGC 2363 V1, $L_{\rm H\alpha} = 10^{38}$ erg s^{-1}; Drissen et al. 2001) $N \sim 7000$, so the resulting p^* is unphysical. Even for the most luminous LBV stars, estimated at $10^{40\text{–}41}$ erg s^{-1} (Guseva et al. 2024), $N = 7$–70, yielding $p^* = 4$–12 per cent; while feasible in theory, systematically attaining such large polarisations for random orientations (averaging at 60°) would exceed the corresponding Chandrasekhar limit of $p^* \simeq 2.8$ per cent (Chandrasekhar 1960). More decisively, when star clusters are polarised, this is usually explained by external polarisation (e.g., Bijas et al. 2022). But because this mechanism operates outside of both the continuum and broad lines, it cannot produce the line effect observed across broad H α. Therefore, our data leave one single, dominant source as the most natural explanation for the optical continuum.

We stress that since our spectropolarimetry covers only the rest-frame optical ($\simeq$ 5300–6650 Å), it provides no new constraints on the ongoing debate about the origin of the rest-frame UV continuum: whether it is host- or AGN-dominated (e.g. Naidu et al. 2025; de Graaff et al. 2025; Sun et al. 2026; D'Eugenio et al. 2025; Torralba et al. 2026; Pérez-González et al. 2026; Geris et al. 2026). Equally, because we do not cover [O III]λλ4959,5007, we cannot test the compact scenario recently proposed to explain short-timescale variability in an LRD at $z = 6.7$ (Lambrides et al. 2026a).

4.3.2 A direct view of the dominant optical continuum source

Having established that a single source dominates the optical continuum (Section 4.3.1), we can now ask whether we view this source directly (as in, e.g., type-1 AGN), or only via scattered light (as in, e.g., type-2 AGN).

We first address the extreme case, in which the observed continuum is entirely scattered light: a single hidden continuum source, seen only via a scattering 'mirror'. The observed level of polarisation disfavours this scenario: purely reflected light is expected to be highly polarised for generic scattering geometries (Section 4.2), well above our observed $p_{\rm cont} \simeq 1.5$ per cent. While some Seyfert-2 nuclei with low observed polarisation do exist, their low p is dominated by dilution from unpolarised host starlight within the aperture; when starlight is subtracted, the remaining scattered nuclear light is highly polarised ($p = 3$–10 per cent; e.g., Tran 1995). This dilution channel is impossible in J1025, whose optical continuum is not host-galaxy light (Ji et al. 2025; Naidu et al. 2025; de Graaff et al. 2025; for J1025 itself, see Lin et al. 2026; Ji et al. 2026c), so a reflection-dominated view would require strong geometric cancellation, i.e., a finely tuned, nearly axisymmetric mirror viewed close to face-on.

Even though we disfavour a reflection-only view of the continuum, a composite scenario is still possible, such as a two-component continuum, in which an unpolarised source dominates the total flux, while a second component, hidden from direct view, is seen only in scattered (hence polarised) light. This hypothesis has concrete realisations among proposed LRD models, for example an unpolarised thermal or nebular continuum seen directly, plus an accretion disc seen only through scattering (e.g., Lin et al. 2026). Polarimetry disfavours this scenario too, because the polarised flux $p \times I$ has nearly the same spectral shape as the total continuum (Fig. 2f). If the two hypothesised continuum components had different natures, the hidden component would need to mimic, across our full wavelength range, the spectral shape of the physically different, dominant source – which would be a remarkable coincidence. Still, we caution that two moderately different continua could still match in shape within our uncertainties, given the short wavelength baseline.

We conclude that the total-light and the polarised-light continua most likely arise from a single dominant component, viewed at least in part directly. This, however does not constrain the nature of the source, nor which mechanism polarises it, which we address next.

4.3.3 Origin of the optical continuum and its polarisation

We now ask what polarises the optical continuum. Having established a single, dominant source (Section 4.3.1), the answer depends on the nature of the continuum source, so we address it separately for three limiting continuum scenarios: nebular dominated, thermal photosphere, and accretion disc.

In a nebular-dominated scenario (e.g., Sneppen et al. 2026b), where the continuum and broad H α arise from recombination in the same ionised gas, any polarisation mechanism would imprint nearly the same polarisation on both continuum and line. So the observed contrast in both p and ϑ rules out this scenario for J1025. For similar reasons, we can also exclude, for J1025, a Compton-thick shell in which the light from a central engine is thermalised by the same gas that produces H α. Variants in which a nebular continuum or the recombination lines are subject to partial reprocessing (e.g., Sneppen et al. 2026b) are not ruled out outright in terms of polarised fraction (due to a possible role of non-scattering opacities and RT effects), but remain strongly disfavoured by the polarisation angle (Sections 4.4 and 4.5), clearly indicating that continuum and line arise from different structures, at least in J1025.

For a thermal photosphere, intrinsic polarisation is not expected at the observed level. There are two reasons. First, in a cold photosphere ($T \sim 5000$ K; Lin et al. 2026), the dominant polarisation mechanism is Rayleigh scattering, but we see no evidence of the corresponding steep blue rise in our polarisation curve (e.g., Fig. 3c; Aurière et al. 2016). Second, at least to the extent that blackbody models are assumed to be nearly spherical (Begelman & Dexter 2026; Kido et al.

2025; Liu et al. 2025)[2], any scattering-induced polarisation undergoes strong geometric cancellation, so the net intrinsic polarisation is expected to be low. On the other hand, non-negligible flattening due to rapid rotation may lead to some polarisation, a quantification of which is beyond the scope of this work (see also Section 4.7.2 below for some known examples of polarised thermal photospheres). External electron- or dust-scattering in a compact region near the source is in principle a natural polariser; thus, even a perfectly spherical photosphere can acquire the observed $p_{\rm cont}$ this way. The expected rise of the polarised fraction towards the blue is not observed, mildly disfavouring dust, although the short baseline cannot conclusively exclude it (Section 4.2 and Appendix B). Since the external scatterer also intercepts the broad line, invoking this mechanism for the continuum must carefully account for the polarisation properties of the broad line too (Section 4.5). Dichroic dust polarisation could also explain the observations. However, thermalised models are often invoked to explain the red optical continuum of LRDs as a low-temperature effect, as opposed to dust reddening (Kido et al. 2025; Liu et al. 2025). Therefore, invoking substantial dichroic-dust polarisation would reintroduce the dust column that this scenario is designed to avoid. Quantitatively, to achieve the observed $p_{\rm cont} = 1.5$ per cent, dichroic polarisation would require $A_V > 0.5$ mag (under the maximum efficiency of Serkowski et al. 1975), and possibly much larger columns for the lower efficiencies commonly inferred for AGN dust (Section 4.2), disfavouring this mechanism.

Finally, a hot, optically thick accretion disc (possibly attenuated by dust or dense gas, Inayoshi & Maiolino 2025; Ji et al. 2025; Naidu et al. 2025; Torralba et al. 2026; Pacucci et al. 2026) is subject to intrinsic polarisation due to electron scattering within its own atmosphere (Section 4.2). Because a disc is flattened, per-cent-level polarisation follows from its geometry alone, increasing with inclination, so our measured $p_{\rm cont} \simeq 1.5$ per cent is most naturally accommodated by an inclined viewing angle. For a semi-infinite, pure-scattering atmosphere, the maximum polarised fraction is $p = 11.7$ per cent for $i = 90°$, decreasing to $p \simeq 1.5$ per cent for an inclination angle $i \simeq 45°$ (Chandrasekhar 1960), although this value should be viewed as a lower limit, since multiple physical effects can act to decrease intrinsic polarisation already at $i = 90°$ (Section 4.2). We note that even an inclination much higher than $i = 45°$ does not conflict with the direct view established in Section 4.3.2, because the relatively modest dust columns inferred for LRDs (ranging from $A_V = 0\ mag$ for the models of Naidu et al. (2025); Torralba et al. (2026), to $A_V \simeq 0.5$–5 mag for the models of Madau & Maiolino 2026; Brazzini et al. 2026; Ji et al. 2026a; Pacucci et al. 2026, as opposed to $A_V \simeq 20$–40 mag in type-2 AGN; e.g., Young et al. 1995; Lumsden et al. 1999) leave the intrinsic optical continuum from the accretion disc unattenuated, or mildly attenuated but still visible (Madau & Maiolino 2026). While intrinsic polarisation is natural for this model, external electron- or dust-scattering contributions are also viable mechanisms, subject to the same caveats as for the thermalised photosphere model. Dichroic polarisation is possible as well, and – unlike for thermalised models – accretion discs can accommodate (and in fact often invoke) dust along the line of sight. Although, in the context of an accretion disc model, dust should generally be regarded as a possible additional contributor, rather than the main agent, of continuum polarisation.

In summary, the total-light and polarised-light continua likely arise from the same, single dominant component (Sections 4.3.1 and 4.3.2). Among the scenarios, nebular continuum alone is ruled out for J1025; a nearly spherical thermal photosphere with $T \simeq 5000$ K seems also disfavoured for lack of the characteristic Rayleigh-scattering signature at relatively blue wavelengths. While viable for all scenarios, external scattering is subject to additional constraints from the broad-line properties, which we discuss next. This leaves an intrinsically polarised accretion disc as the simplest framework.

[2] The truncated-disc version of the Liu et al. 2025 model is geometrically closer to an accretion disc compared to the other blackbody models.

4.4 The angle offset requires broken axial symmetry

One conclusion is independent of which polarisation mechanisms operate: whatever polarises the line or the continuum, an axisymmetric configuration can only produce polarisation angles of 0° or 90° with respect to the projection of the symmetry axis in the plane of the sky, so the observed intermediate ϑ offset (Section 3.4 and Table 1) requires broken axial symmetry (e.g., Goosmann & Gaskell 2007). The basic argument is very general. In a coordinate system (Q', U') aligned with the symmetry axis of the system, the assumed axial symmetry implies a symmetry by reflection in the plane defined by the symmetry axis and the line of sight, which prohibits values of (wavelength-integrated) U' different from 0 and therefore polarisation angles different from 0° or 90°.

For instance: in the case of internal electron scattering, the expected polarised fraction depends on both the flattening and the optical depth of the emitting surface, as well as the line of sight to the observer (Angel 1969). A gradual change in optical depth corresponds to a gradual change in Q' from positive to negative values, while U' is always zero for symmetry reasons. As a result, local maxima of the polarised fraction are achieved in the optically thin and thick limits, with a shift of 90° in polarisation angle between the two, while zero polarisation is in general achieved at some intermediate optical depth, whose value depends on the axis ratio and viewing angle. Crucially, for an axisymmetric system, there is no value of the optical depth and no line of sight towards which the emitted light can have a wavelength-integrated polarisation angle different from 0° or 90° with respect to the projected symmetry axis. Therefore, if both the continuum and the BLR are separately polarised by internal scattering in an axisymmetric structure, we must conclude that the two structures are strongly misaligned (by $\sim$ 40–50°) with respect to one another.

Similarly, external scattering (by either ionised gas or dust) can produce intermediate polarisation angles only if the scatterer does not share the same symmetry axis as the source, while dichroic transmission requires the magnetic field to be misaligned.

As a first but very general conclusion, we can exclude, at least for J1025, a dust-free homogeneous spherical configuration, as well as any combination of nested aligned axisymmetric structures without dust. Removing any one or more of these assumptions opens the door to possible solutions.

We identify three general symmetry-breaking mechanisms, which we will use in the following: a line-emitting or line-scattering structure inclined with respect to the axis of the continuum polariser; large-scale clumpiness or irregularity of the line-emitting or scattering medium; and dichroic transmission through an external dust screen whose grain-aligning magnetic field is misaligned with the continuum polarisation axis.

4.5 BLR geometry and polarisation

Different models have been proposed for the geometry and nature of the BLR in LRDs, based on several partially interconnected questions: (i) is the BLR a rotating disc, or is it more similar to a quasi-spherical structure? (ii) What physical processes are responsible for the broadening of the lines? (iii) Is the BLR physically related to the dense gas absorbers detected in Balmer emission lines? (iv) Is the BLR related to the mechanism responsible for the reddening of the optical continuum in LRDs compared to ordinary AGN? And (v) how to explain the similarities and differences between LRDs and LBDs[3]?

Here below we discuss what our polarisation measurements tell us about the first (geometrical) question. The second, partially related question about the broadening mechanism is discussed in Section 4.6. The other questions are touched upon when relevant, although addressing all of them in a complete and exhaustive way is beyond the scope of this work.

4.5.1 *Quasi-spherical BLR*

A perfectly spherical, homogeneous BLR cannot be intrinsically polarised, from symmetry. To be consistent with our data, a model of this kind requires an external polariser (electron or dust scattering, or dichroic transmission), which must also be misaligned with respect to the polarisation axis of the continuum. Similar to what discussed for the continuum (Section 4.3.3), achieving the observed $p_{\mathrm{H}\,\alpha} = 0.58$–$0.84$ by dichroic transmission requires a dust attenuation of at least $A_V \simeq 0.2$–0.4 mag, assuming the maximum theoretical efficiency of 3 per cent mag^{-1} (Section 4.2), or significantly higher levels ($A_V \simeq 2$–5 mag) if a typical AGN efficiency of 0.1-0.3 per cent mag^{-1} (see Section 4.2) is assumed. Note that, in the current literature, spherical BLR configurations are generally proposed together with the assumption of dust-free screens, and the high observed Balmer decrements are driven primarily by collisional excitation and/or radiative transfer effects (e.g., Chang et al. 2026; Matthee et al. 2026). So while possible, the dust solution does not match any of the currently proposed models to our knowledge.

On the other hand, a quasi-spherical BLR does not need to be exactly spherical, but may have some flattening. Also, recent quasi-spherical BLR models of LRDs tend to have a non-homogeneous structure, with thick inflows on the equator and thin outflows on the poles (Sneppen et al. 2026a; Matthee et al. 2026). This may be related to the LRDs/LBDs phenomenology (Matthee et al. 2026). Models of this kind have a preferred direction; therefore, in addition to external polarisation mechanisms (as above), they may also have intrinsic polarisation due to internal scattering. Note that internal scattering may also be related to the BLR broadening mechanism (Section 4.6.1). The exact polarised fraction then depends on many factors (flattening, latitudinal structure, optical depth, line of sight), so a quantitative assessment would require a dedicated theoretical study and is left for future work. A robust conclusion for J1025 is that, if intrinsic polarisation of a quasi-spherical BLR dominates, then the preferred axis of the BLR must have a strong (40–50°) misalignment with respect to the symmetry axis of the continuum.

4.5.2 *Rotating disc*

We now discuss the implications of our polarisation measurements for a scenario in which the BLR of J1025 is a rotating disc. We keep the discussion general, but we note at the start that a rotating disc is invoked, in particular, by the unification model proposed by Madau & Maiolino (2026). Like the Matthee et al. (2026) model, the Madau & Maiolino (2026) model also addresses the LRD/LBD dichotomy, but this time invoking dust (rather than just dense gas) being concentrated along the equator, more similar to the classical unification model of ordinary AGNs (Antonucci 1993; Urry & Padovani 1995). Further similarities and differences with the classical AGN unification model are discussed in Section 4.7, while implications for the line broadening mechanism are left for Section 4.6.2. Here we focus on polarisation and geometry.

Because a rotating disc is highly flattened, intrinsic polarisation is possible, and actually likely. If this is the dominant mechanism, however, the observed line-to-continuum offset in polarisation angle requires the BLR disc to be strongly tilted (∼ 40–50°) compared to the accretion disc, just as discussed in Section 4.5.1.

Scattering by an external ionised medium is also possible. However, satisfying the broken symmetry requires that the scatterer be out of axis. We should also in general expect that the same ionised gas will scatter and polarise light from the accretion disc as well, in which case it must be in an opportune 3D position to intercept the BLR and the continuum with vastly different angles, as observed. In particular, the distance of the scatterer from the central source cannot be much larger than that of the BLR, otherwise both BLR and continuum would be seen under a similar scattering angle.

Dust scattering is an appealing option for a rotating disc, because it can break the axial symmetry *locally*, i.e. at each wavelength: this produces a blue-to-red angle swing for pure rotation (Smith et al. 2005), or an M-shaped angle structure for rotation plus a wind (Lira et al. 2021). Neither, however, produces a global, velocity-integrated offset like that in J1025 unless the *global* axial symmetry is also broken — by a dust plane or wind misaligned with the disc, or by large-scale clumpiness that samples the scattering geometry incompletely (Smith et al. 2005). In all cases, dust scattering requires a line of sight that does not pass through the dust screen; it is therefore disfavoured for J1025 within the Madau & Maiolino (2026) model, in which a red LRD such as J1025 is seen precisely *through* the screen.

Dichroic transmission through a dust screen with misaligned magnetic field is not only possible, but in fact natural: within the Madau & Maiolino (2026) framework, a red object like J1025 needs a dust screen as an intrinsic model component, rather than an *ad-hoc* addition. From the observed $p_{\mathrm{H}\,\alpha}$, we derive the same dust attenuation as for the spherical BLR models, but this time $A_V = 2$–5 mag aligns very well with the model's requirements. As a consistency check, taking the broad line to be intrinsically unpolarised and to carry only the screen term, $p_{\mathrm{d}} \simeq 0.58$ per cent at $\vartheta_{\mathrm{d}} \simeq -34°$, and subtracting this term in Stokes space from the observed continuum polarisation, the intrinsic continuum polarisation is $\simeq 1.7$ per cent at $\vartheta \simeq +22°$: thus the screen slightly rotates and slightly reduces the intrinsic disc polarisation, without cancelling it – all within the reasonable polarisation efficiency budget of $dp/dA_V \simeq 0.1$–0.3 per cent mag^{-1}. Finally, the misalignment between the two polarisers arises naturally, because the grain-aligning magnetic field does not need to share the orientation of the nuclear disc axis (Balbus & Hawley 1991): the broken axial symmetry is then expected, rather than fine-tuned. We recall that the presence of significant dust extinction in some LRDs has been challenged by the lack of corresponding emission in the MIR (e.g., Setton et al. 2025a), but this assumes isotropic dust coverage and may not apply if extinction occurs only along specific lines of sight.

[3] Acronym for 'Little Blue Dots', with some similarities with LRDs, but no Balmer break and overall bluer SEDs, see e.g. Brazzini et al. (2026)

4.5.3 Irregular or chaotic BLR

Finally, the BLR itself might be highly irregular or chaotic. The observed signal in this case could arise from a structure lacking any special symmetry and dominated by one or more large clumps with a random orientation with respect to the accretion disc and our line of sight. A scenario of this kind could easily explain a large angle offset, regardless of the exact polarisation (or broadening) mechanism. On the other hand, it may not be easy, within this framework, to explain the absence of a similarly strong velocity offset of the BLR emission from the systemic velocity, or the low observed levels of variability (Zhang et al. 2025; Burke et al. 2026; Liu et al. 2026, but see Ji et al. 2025; Furtak et al. 2025; Lambrides et al. 2026a for a different view). We refrain from further speculation in this regard, as to our knowledge models of this kind are so far absent from the LRD literature, but may be worth some investigation in the light of our measurement for J1025. A larger sample of LRDs with spectropolarimetry could certainly also be helpful in this respect. Within a chaotic model, the key prediction is that different objects should have a wide variety of angle offsets, with a random, or close to random, distribution.

4.6 Line broadening mechanism

We now turn from what polarises the broad line to what broadens it, discussing two contrasting limits: microscopic broadening by electron scattering (Rusakov et al. 2026), and kinematic broadening by virial motions (e.g., Juodžbalis et al. 2026b). Beyond the physical understanding of LRDs (and other exponential-wing AGN; Brazzini et al. 2026), the distinction bears directly on the inferred mass of the central black hole and its accretion rate (Maiolino et al. 2024; Rusakov et al. 2026), with a profound impact on black-hole seeding and growth.

It is also useful to recall that non-Gaussian line profiles (including exponential wings) are not unique to LRDs, but are seen in blue AGN (Brazzini et al. 2026) and in luminous quasars (e.g., Nagao et al. 2006; Kollatschny & Zetzl 2013, Trefoloni, in prep.). Both virial motions and electron scattering have been discussed, prior to the discovery of LRDs, in the literature on line broadening for ordinary AGN (e.g. Laor 2006).

4.6.1 Electron-scattering broadening

In the electron-scattering scenario, H α is broadened by a scattering medium either co-spatial with the H α production site (Torralba et al. 2026), or interposed between the BLR and the observer at least along our line of sight (Rusakov et al. 2026).

In the recent literature, electron-scattering broadening is often invoked by quasi-spherical BLR models, although in principle it could apply to disc or irregular morphologies as well. Regardless of the exact geometry, for small optical depths $\tau_e \lesssim 1$ this mechanism predicts that $p \times I$ be broader than I, because photons in the exponential wings have been scattered and hence polarised, while those in the unscattered core should not be polarised. This effect is seen, for example, in NGC 1068, where broad H α viewed through electron-scattering regions is substantially broader than the same line viewed through dust-scattering ones (Miller et al. 1991). Although promising in principle, the discriminatory power of this test is unfortunately quite limited in J1025. This is because, within the scattering-broadening model, a prominent exponential wing (as in J1025) is only possible as a result of a relatively large τ_e ($\gtrsim 1$), which in turn implies a large suppression ($e^{-\tau_e}$) of the unpolarised core signal. Further difficulties arise from contamination of the line core by absorption features, and by the narrow-line region and host galaxy, which may or may not be polarised by an independent mechanism. Quantitatively, our data are consistent with the width of polarised and total light being the same (Section 3.5), as well as with a toy scattering model (Section 3.6), with residuals indicative of complex structures near line core. We cannot therefore reach a clear conclusion on this matter based on our data, but we note that further progress could be made by targeting with high SNR objects with a larger core-to-wing ratio, no prominent absorption features and no evidence of a spatially resolved NLR.

We recall that our toy electron-scattering fit (Section 3.6) requires $\tau_e \sim 1$ (constrained by the transmitted-core fraction) and $p \sim 0.8$ per cent (constrained by the polarised flux). In principle, this combination of parameters could be used to put constraints on the required flattening and viewing angle of a hypothetical ellipsoidal cocoon (e.g., Angel 1969). This is left for future investigation. Importantly, we recall that the inferred optical depth is a consequence of fitting exponential wings with a scattering kernel, which, as we discuss below, is not the only possible approach to the problem.

4.6.2 Virial broadening

Electron scattering is not the only mechanism able to produce the exponential line shape of LRDs: recent stratified-BLR models reproduce the same exponential wings as LRDs by purely kinematic broadening, without invoking electron scattering as the primary mechanism (Scholtz et al. 2026; Madau et al. 2026).

In principle, virial broadening is possible in any geometry, including a quasi-spherical configuration, provided that the opacity to electron scattering τ_e is sufficiently small. It is therefore not possible to formulate a completely general prediction of the spectropolarimetric signature of virial broadening. With this caveat in mind, we restrict our attention to the LRD/LBD unification model by Madau & Maiolino (2026), which invokes virial broadening specifically in the context of a rotating disc (see Section 4.5.2). A rotating disc is also among the most widespread virialised models for standard AGN. It is directly observed in some high-luminosity quasars (GRAVITY Collaboration 2018; GRAVITY+ Collaboration 2024, 2026), and inferred in standard AGN from the blue-to-red swing in ϑ across the broad lines (e.g., Smith et al. 2005); this includes some low-luminosity narrow-line Seyfert-1 galaxies, a luminosity regime closer to LRDs like J1025 (e.g., Afanasiev et al. 2019).

Within the Madau & Maiolino (2026) model, the favoured BLR polarisation mechanism for J1025 is dichroic transmission (Section 4.5), whose efficiency is achromatic across the line and therefore implies identical $p \times I$ and I widths. This is consistent with our results, although, as mentioned in Section 4.6.1, we cannot consider this as a decisive proof in favour of one particular broadening mechanism.

In addition to targeting other objects with a larger core-to-wing ratio, the Madau & Maiolino (2026) model could also be tested by targeting LBDs, for which the favourite polarisation mechanism would be equatorial dust scattering and the distinctive feature would be a blue-to-red swing in polarisation angle, without a systematic (angle-integrated) offset. A detected swing would be transformative, as it would both confirm the origin of the line broadening and open an independent avenue for measuring the black-hole mass (Afanasiev & Popović 2015).

4.7 Phenomenological analogies

Having discussed the physical constraints, and before presenting a synthesis (Section 4.8), we now step back to ask where comparable polarisation signatures have been observed. On their own, these phenomenological analogies are not conclusive; still, they show that neither the continuum-to-line depolarisation nor the large angle offset are unique to J1025– even though no single object class reproduces the full combination.

4.7.1 *Type-1 AGN spectropolarimetry*

Since LRDs have broad Balmer lines, the closest phenomenological comparison is with type-1 AGN spectropolarimetry. In the Seyfert sequence discussed by Smith et al. (2002, 2004, 2005), equatorial-scattering Seyfert 1 nuclei can show a blue-to-red swing in polarisation angle across broad lines, while polar-scattered Seyfert 1 nuclei (Smith et al. 2004) show stronger continuum polarisation and Seyfert-2 scattering signatures. Near face-on systems can have low net polarisation because of azimuthal cancellation.

While J1025 does not fully match any one of these limiting cases, type-1 AGN show remarkable object-to-object diversity (Smith et al. 2002, 2004): broad-line depolarisation, core dips, and wing polarisation are all common in type-1 AGN, so J1025 would not be unique, in this respect. The closest analogue of J1025 in polarisation is Mrk 279, which displays both depolarised H α relative to the continuum, and different polarisation angle between continuum and H α (evaluated without continuum subtraction), $\Delta\vartheta \simeq 61°$ (Smith et al. 2002). However, the total-light picture is completely different, as Mrk 279 is X-ray bright (Costantini et al. 2007) and time variable (Bachev & Strigachev 2004).

Especially interesting analogues are narrow-line Seyfert-1 galaxies (NLSy1), which can show broad-line depolarisation and complex line-profile behaviour (Goodrich 1989; Smith et al. 2002). The comparison with NLSy1 is also interesting for other reasons. Due to their relatively narrow broad lines, it is easier to identify the signatures of electron-scattering broadening (Laor 2006). Relatively narrow and forbidden Fe II emission was first identified in 1 Zw I (Véron-Cetty et al. 2004), and recently discovered in LRDs at both low and high redshifts (e.g., Lin et al. 2026; Ji et al. 2026c at $z \lesssim 0.2$; Tripodi et al. 2025; D'Eugenio et al. 2025; Torralba et al. 2026 at z = 5–7). Finally, the NLSy1 Akn-564 is the nearest nitrogen-loud AGN (Yang et al. 2025), echoing the high nitrogen abundance in some LRDs (Ji et al. 2026b) and LBDs (Ji et al. 2024). Still, Smith et al. (2002) argue that NLSy1s do not form a single polarimetric family, and that their H α polarisation properties are indistinguishable from those of ordinary Seyfert-1 galaxies. In our case, we can take the strong object-to-object differences within the same AGN sub-classes as a warning that a single observation is unlikely to be representative of the entire LRD class.

In the unification model of Madau & Maiolino (2026), LRDs are the obscured counterparts of LBDs, consistent with the dichroic-screen picture for J1025 (Section 4.5.2). The polarisation nonetheless differs from classical type-2 (Seyfert-2) nuclei, in which the broad lines, seen only in scattered light, are at least as polarised as the continuum (Antonucci & Miller 1985; Smith et al. 2002; Tran 2003), unlike the depolarised broad H α in J1025; this is natural if J1025 is instead viewed through modest, dichroic obscuration rather than through equatorial or polar scattering, unlike in classical type-2 AGN.

A final useful AGN comparison is with the quasars studied by Kishimoto et al. (2004, 2005, 2008), in which the polarised flux is dominated by the continuum and the broad lines are strongly suppressed. In objects like Ton 202 (Kishimoto et al. 2003), the detection of a 'Balmer-edge' feature in polarised light echoes the observations of LRDs in direct light (Labbe et al. 2024; Setton et al. 2025b).

4.7.2 *Emission-line stars*

Emission-line stars offer an instructive phenomenological analogy, though we stress that the physical drivers, energy source, and scales differ entirely from those of J1025 (as we quantify at the end of this section).

In several classes of line-emitting stars, such as Herbig Ae, Be and B[e] stars, as well as luminous blue variables (LBVs), the continuum is intrinsically polarised due to a flattened geometry, interpreted as an accretion or decretion disc (for Herbig stars, Vink et al. 2002) or the stellar surface itself (for LBVs, Davies et al. 2005). H α is often found to be polarised differently from the continuum, including several examples of depolarised lines, especially among Herbig Be stars (Vink et al. 2002) and LBVs (Davies et al. 2005), similar to the depolarisation pattern we observe in J1025. Line depolarisation in Herbig Be stars has been interpreted as a signature of the line forming over a less flattened, more symmetric volume compared to the continuum (Oudmaijer & Drew 1999; Vink et al. 2002). For some of the Herbig Be stars and LBVs with depolarised H α, there is also a measurable angle offset, although it is usually modest ($\lesssim$ 10 deg).[4] For Herbig Be stars, Oudmaijer & Drew (1999) attribute the H α polarisation angle offset to superimposed interstellar and circumstellar dust polarisation over an otherwise unpolarised line, which matches our dichroic scenario. In the LBVs of Davies et al. (2005), line polarisation is instead considered to be intrinsic and is thought to trace wind asphericity and clumpiness. Furthermore, the polarisation angle in these objects is found to be variable with time, over a timescale of decades (Davies et al. 2005), reinforcing an interpretation of asphericity and clumpiness in their stellar winds. This erratic behaviour is not unexpected given the violent, spatially complex mass-loss phenomena known to occur in these systems, resonating with the 'chaotic BLR' scenario briefly sketched in Section 4.5.3 (see also Naidu et al. 2026 for a differently flavoured analogy between LBVs and LRDs). Overall, there are interesting similarities between the polarisation properties of emission-line stars and J1025, although we have found no example that matches exactly the pattern we observe in our target.

Besides these similarities, it should be recalled that these classes of stars are a disparate set of systems, ranging from pre-main sequence objects, to late-stage intermediate-mass stars, to very massive stars on the main-sequence. The structural analogy is however suggestive: the fact that such a diverse set of objects can still present a large number of common spectral properties suggests that the underlying physical structure and processes are not unique, and to the contrary must be relatively easy to attain. One such model is the classic B[e]-star picture of Zickgraf et al. (1985, 1986): a fast polar wind pinched by a slow, dense equatorial flow, the stellar analogue of an outflow pinched by an accretion disc, reminiscent of the inflow/outflow model proposed for LRDs (Sneppen et al. 2026a; Matthee et al. 2026). In Zickgraf's model, the disc generates high auroral-to-nebular line ratios by collisional excitation in very dense, low-ionization gas (e.g., auroral [S II]λλ4069,4071,6731, [N II]λ5755), also observed in LRDs (Ji et al. 2026c; D'Eugenio et al. 2025). These parallels motivate emission-line stars as a phenomenological point of comparison (not a physical model) for some of the processes at play in LRDs (Appendix D).

Nevertheless, the luminosity, physical scale, and power source of J1025 are those of an accretion-powered source, not of a nuclear-powered one. As discussed in Section 4.3.1, J1025 is 7000 times more

[4] We note, however, that larger offsets are sometimes found in emission-line stars where H α is over-polarised, or has an irregular polarisation pattern, relative to the continuum (Vink et al. 2002).

luminous in H α than the most luminous emission-line star (Drissen et al. 2001), and 7–70 times more luminous than candidate LBV stars in metal-poor starburst dwarf galaxies (Guseva et al. 2024). For high-luminosity LRDs (Wang et al. 2024; Juodžbalis et al. 2024; Labbe et al. 2024), the flux mismatch rises to several orders of magnitude.

4.8 A preferred picture for J1025 and an outlook

Our preferred (but not unique) interpretation is the simplest one surviving the constraints of Sections 4.3.3 and 4.5: the continuum is not nebular dominated, and is polarised intrinsically, as expected for an accretion disc; most broad-H α emission arises over a larger region, which is either inclined with respect to the continuum polariser or seen through a misaligned dichroic dust screen. This naturally explains why the continuum is more polarised than broad H α, and why the broad line has a weak but distinct polarisation angle.

If framed within the unification scheme by Madau & Maiolino (2026), the easiest solution for the symmetry break is dichroic polarisation of the BLR by a magnetised dust screen, with a misaligned magnetic field. In this picture, the key difference with respect to standard type-1 AGN is a modest dust obscuration ($A_V \simeq 2$–5 mag). In particular, in this interpretation, J1025 is geometrically type-2-like – obscured and reddened – but with a much weaker obscuring torus compared to classical type-2 AGN ($A_V \gtrsim 20$ mag). The much smaller dust column does not hide the broad lines nor the accretion-disc continuum, so the type-1 signatures, and features such as the Balmer break, appear in direct light rather than only in polarised light.

More in general, our findings are consistent with a broader LRD/LBD picture in which a central compact nuclear structure manifests itself as an LRD or an LBD along different lines of sight, as a consequence of orientation effects and in particular different columns of either dense gas (Matthee et al. 2026) or dust (Madau & Maiolino 2026), or both.

Our polarimetry data do not rule out a quasi-spherical cocoon, but symmetry breaking means that the model must be more complex than a nearly spherical shell, so that the BLR must have a preferred axis (by either flattening or latitudinal stratification of gas column density) which differs markedly from the symmetry axis of the continuum. Alternatively, an aligned or even spherical cocoon could also be reconciled with the data by invoking dichroic polarisation through a magnetised dust screen, with $A_V \sim 2$–5 mag (Section 4.5.1).

A highly irregular geometry of the BLR, characterised by e.g. chaotic accretion, large-scale granularity and no special symmetry could also be a route to explain our data, although it may be in contrast with other constraints (Section 4.5.3) and certainly requires a statistical sample to be further investigated.

As for what broadens the line, both electron scattering and virial motions are consistent with our data: the exponential wing widths of the polarised and total flux are statistically indistinguishable (Section 4.6).

A larger sample would help to better constrain the polarisation mechanisms in LRDs, as well as LBDs. For the scenario of dichroic transmission, more data would allow to test the prediction that BLR polarisation without angle swings should occur mainly along lines of sight typical of LRDs and not along those of LBDs (Madau & Maiolino 2026; Brazzini et al. 2026). At the same time, the dust scattering mechanism from a rotating BLR could instead be revealed by the measurement of the angle-swing signature in relatively face-on LBDs (Section 4.6.2). Finally, more measurements of differential widths of polarised and total-intensity lines for objects with different core-to-total fraction would help to put stringent constraints on electron-scattering as a viable broadening mechanism (Section 4.6.1).

5 CONCLUSIONS

We have presented VLT/FORS2 optical linear spectropolarimetry of the local Little Red Dot J1025 ($z \simeq 0.1$; 'Lord of LRDs', Ji et al. 2026c; 'The Egg', Lin et al. 2026), spanning rest-frame ∼ 5300–6650 Å.

- The continuum near H α is polarised at $p_{\rm cont} \simeq 1.5$ per cent, with polarisation angle $\vartheta_{\rm cont} \simeq +12°$. $p_{\rm cont}$ is comparable to some intrinsically polarised Seyfert-1 nuclei. A purely Galactic foreground origin is excluded, so the polarisation is intrinsic to J1025 and points to a single, dominant continuum source rather than to many stellar sources.
- Broad H α is also polarised, but less than the continuum ($p_{\rm H\,\alpha} =$ 0.58–0.84 per cent). Pure dilution by an intrinsically unpolarised line does not fully explain the data: the continuum-subtracted line shows a significant polarisation-angle offset from the continuum, $\Delta\vartheta \simeq -48°$ (line PA $\vartheta_{\rm H\,\alpha} = -34 \pm 3°$). Continuum and broad-line are produced in different locations and further require a break of axial symmetry in the system.
- The continuum polarisation is only weakly chromatic ($dp/d\lambda \simeq -0.26 \pm 0.15$ per cent per rest-frame 1000 Å), so the present optical data do not single out intrinsic disc polarisation, dust, or grey electron scattering as the dominant continuum-polarising channel.
- The H α profile in polarised light is not detectably broader than the profile in total light: modelling the narrow polarised core, the exponential wing width of the polarised flux is $W_{p\times I} = 490 \pm 130$ km s^{-1}, statistically consistent with $W_I = 550 \pm 10$ km s^{-1} from the total-light fit, but the large errorbars on $W_{p\times I}$ make the width test unconstraining.
- We derive a robust geometric constraint: the strong line angle offset requires broken axial symmetry; suitable symmetry breaking mechanisms are a broad-line emitting or scattering region misaligned relative to the continuum, an asymmetric external scattering mirror, or dichroic dust transmission, with the grain-aligning magnetic field misaligned relative to the continuum polarisation axis.

Taken together, the simplest surviving interpretation (Section 4.8) is a continuum intrinsically polarised in a compact, flattened region, with broad H α forming over a larger volume and polarised along a different axis; the nebular-dominated continuum is ruled out, and any line-scattering medium must be inhomogeneous, or misaligned with respect to the symmetry axis of the continuum source. Both virial motions and electron scattering are consistent with the data; deeper spectropolarimetry of J1025 and a sample of local LRDs can rule out one or the other scenario.

Future spectropolarimetric observations on larger samples will also be crucial to determine whether the symmetry break we identified in J1025 is unique to this object or a general property of the LRD (and possibly LBD) population. If an asymmetry is found to be common, a systematic study of the relation (or lack thereof) of the line-continuum polarisation angle offset with other properties (e.g., broad-band spectrum, line shape) could shed light on the geometry and ultimate nature of this mysterious class of objects.

ACKNOWLEDGEMENTS

Based on observations made with ESO Telescopes at the La Silla Paranal Observatory under programme ID 115.29FY. We are grateful to the ESO Director General, Xavier Barcons, for awarding Director's Discretionary Time for this programme, and to Dr Henri M. J. Boffin and the Paranal observatory staff for their support in executing the observations. FDE, RM, XJ, JS, IJ, and RGP acknowledge support by the Science and Technology Facilities Council (STFC), by the ERC through Advanced Grant 695671 "QUENCH", and by the UKRI Frontier Research grant RISEandFALL. RM also acknowledges funding from a research professorship from the Royal Society. AM acknowledges the MIRACLE INAF 2024 GO grant "A JWST/MIRI MIRACLE: Mid-IR Activity of Circumnuclear Line Emission", the INAF Large Grant 2022 "The metal circle: a new sharp view of the baryon cycle up to Cosmic Dawn with the latest generation IFU facilities", the grant PRIN-MUR 2020ACSP5K_002 financed by European Union – Next Generation EU, and project PRIN-MUR project "PROMETEUS" financed by the European Union – Next Generation EU, Mission 4 Component 1 CUP B53D2300475000. CRA acknowledges support from the Agencia Estatal de Investigación of the Ministerio de Ciencia, Innovación y Universidades (MCIU/AEI) under the grant "Tracking active galactic nuclei feedback from parsec to kiloparsec scales", with reference PID2022−141105NB−I00 and the European Regional Development Fund (ERDF). XL and XF acknowledge support from the NSF grant AST-2308258. MB acknowledges support from the Next Generation EU funds within the National Recovery and Resilience Plan (PNRR), Mission 4 - Education and Research, Component 2 - From Research to Business (M4C2), Investment Line 3.1 - Strengthening and creation of Research Infrastructures, Project IR0000034 – "STILES - Strengthening the Italian Leadership in ELT and SKA". ZC acknowledges support from the National Key R&D Program of China (grant no. 2023YFA1605600), the National Natural Science Foundation of China (#12525303), the Tsinghua University Initiative Scientific Research Program, and the New Cornerstone Science Foundation through the XPLORER PRIZE. SC acknowledges support by European Union's HE ERC Starting Grant No. 101040227 – WINGS. IJ also acknowledges support by the Huo Family Foundation through a P.C. Ho PhD Studentship. ST acknowledges support by the Royal Society Research Grant G125142. FS acknowledges support from NSF award AST-2513040.

This work made extensive use of the freely available Debian GNU/Linux operating system. We used the Python programming language (van Rossum 1995), maintained and distributed by the Python Software Foundation. We made direct use of Python packages ASTROPY (Astropy Collaboration et al. 2013, 2018), CORNER (Foreman-Mackey 2016), EMCEE (Foreman-Mackey et al. 2013), JWST (Alves de Oliveira et al. 2018), MATPLOTLIB (Hunter 2007), NUMPY (Harris et al. 2020), PROSPECTOR (Johnson et al. 2021) v2.0, PYNEB (Luridiana et al. 2015), PYTHON-FSPS (Johnson et al. 2023), PYSERSIC (Pasha & Miller 2023), QUBESPEC (Scholtz et al. 2025), and SCIPY (Jones et al. 2001). We also used the software packages FSPS (Conroy et al. 2009; Conroy & Gunn 2010), TOPCAT (Taylor 2005), FITSMAP (Hausen & Robertson 2022) and DS9 (Joye & Mandel 2003).

DATA AVAILABILITY

The raw data will be available on the ESO Science Archive Facility, under programme ID 115.29FY.001. The reduced and combined spectra used in this work are publicly available on Zenodo, at https://doi.org/10.5281/zenodo.6926671. The reduced SDSS spectra used for the calibration are available from the SDSS website, at this link. This work has made use of the BeSS database, operated at LESIA, Observatoire de Meudon, France: http://basebe.obspm.fr.

REFERENCES

Ababakr K. M., Oudmaijer R. D., Vink J. S., 2017, MNRAS, 472, 854
Abazajian K. N., et al., 2009, ApJS, 182, 543
Afanasiev V. L., Popović L. Č., 2015, ApJ, 800, L35
Afanasiev V. L., Popović L. Č., Shapovalova A. I., 2019, MNRAS, 482, 4985
Agol E., Blaes O., 1996, MNRAS, 282, 965
Akins H. B., et al., 2025, ApJ, 991, 37
Alves de Oliveira C., et al., 2018, in Observatory Operations: Strategies, Processes, and Systems VII. p. 107040Q (arXiv:1805.06922), doi:10.1117/12.2313839
Ananna T. T., Bogdán Á., Kovács O. E., Natarajan P., Hickox R. C., 2024, ApJ, 969, L18
Andersson B.-G., Lazarian A., Vaillancourt J. E., 2015, ARA&A, 53, 501
Angel J. R. P., 1969, ApJ, 158, 219
Antonucci R., 1993, ARA&A, 31, 473
Antonucci R. R. J., Miller J. S., 1985, ApJ, 297, 621
Archer A., et al., 2025, ApJ, 995, 191
Astropy Collaboration et al., 2013, A&A, 558, A33
Astropy Collaboration et al., 2018, AJ, 156, 123
Aurière M., et al., 2016, A&A, 591, A119
Bachev R., Strigachev A., 2004, Astronomische Nachrichten, 325, 317
Balbus S. A., Hawley J. F., 1991, ApJ, 376, 214
Barro G., Perez-Gonzalez P. G., Kocevski D. D., Leung G. C. K., McGrath E., Somerville R. S., Trump J. R., Yung L. Y. A., 2025, Revealing the True Nature of Little Red Dots with Deep Continuum Observations of an IR-Bright LRD at z=3.1, JWST Proposal. Cycle 4, ID. #8358
Barth A. J., Tran H. D., Brotherton M. S., Filippenko A. V., Ho L. C., van Breugel W., Antonucci R., Goodrich R. W., 1999a, AJ, 118, 1609
Barth A. J., Filippenko A. V., Moran E. C., 1999b, ApJ, 525, 673
Begelman M. C., Dexter J., 2026, ApJ, 996, 48
Bijas N., Eswaraiah C., Wang J.-W., Jose J., Chen W.-P., Li D., Lai S.-P., Ojha D. K., 2022, MNRAS, 515, 3352
Brazzini M., et al., 2026, arXiv e-prints, p. arXiv:2601.22214
Burke C. J., Liu X., Chen Y.-C., Shen Y., Guo H., 2021, MNRAS, 504, 543
Burke C. J., Stone Z., Shen Y., Jiang Y.-F., 2026, ApJ, 1004, 16
Cardelli J. A., Clayton G. C., Mathis J. S., 1989, ApJ, 345, 245
Chandrasekhar S., 1960, Radiative transfer. Dover, New York
Chang S.-J., Gronke M., Matthee J., Mason C., 2026, MNRAS, 545, staf2131
Coleman H. H., Shields G. A., 1990, ApJ, 363, 415
Conroy C., Gunn J. E., 2010, FSPS: Flexible Stellar Population Synthesis, Astrophysics Source Code Library, record ascl:1010.043 (ascl:1010.043)
Conroy C., Gunn J. E., White M., 2009, ApJ, 699, 486
Costantini E., et al., 2007, A&A, 461, 121
D'Eugenio F., et al., 2025, arXiv e-prints, p. arXiv:2510.00101
D'Eugenio F., et al., 2026a, MNRAS, 545, staf2117
D'Eugenio F., et al., 2026b, MNRAS, 547, stag401
Davies B., Oudmaijer R. D., Vink J. S., 2005, A&A, 439, 1107
Delvecchio I., et al., 2025, A&A, 704, A313
Drissen L., Crowther P. A., Smith L. J., Robert C., Roy J.-R., Hillier D. J., 2001, ApJ, 546, 484
Fan X., et al., 2001, AJ, 122, 2833
Foreman-Mackey D., 2016, The Journal of Open Source Software, 1, 24
Foreman-Mackey D., Hogg D. W., Lang D., Goodman J., 2013, PASP, 125, 306
Fosalba P., Lazarian A., Prunet S., Tauber J. A., 2002, ApJ, 564, 762
Furtak L. J., et al., 2024, Nature, 628, 57
Furtak L. J., et al., 2025, A&A, 698, A227
GRAVITY Collaboration 2018, Nature, 563, 657
GRAVITY+ Collaboration 2024, Nature, 627, 281
GRAVITY+ Collaboration 2026, A&A, 706, A99

Geris S., et al., 2026, arXiv e-prints, p. arXiv:2606.21614
Gnedin Y. N., Silant'ev N. A., Shternin P. S., 2005, arXiv e-prints, pp astro–ph/0503121
Goodrich R. W., 1989, ApJ, 342, 224
Goodrich R. W., Miller J. S., 1994, ApJ, 434, 82
Goosmann R. W., Gaskell C. M., 2007, A&A, 465, 129
Greene J. E., et al., 2024, ApJ, 964, 39
Guseva N. G., Thuan T. X., Izotov Y. I., 2024, MNRAS, 527, 3932
Harikane Y., et al., 2023, ApJ, 959, 39
Harris C. R., et al., 2020, Nature, 585, 357
Hausen R., Robertson B. E., 2022, Astronomy and Computing, 39, 100586
Hunter J. D., 2007, Computing in Science and Engineering, 9, 90
Inayoshi K., Maiolino R., 2025, ApJ, 980, L27
Inayoshi K., Visbal E., Haiman Z., 2020, ARA&A, 58, 27
Jaschek C., Andrillat Y., Jaschek M., 1996, A&AS, 117, 281
Ji X., et al., 2024, MNRAS, 535, 881
Ji X., et al., 2025, MNRAS, 544, 3900
Ji X., et al., 2026a, arXiv e-prints, p. arXiv:2604.03370
Ji X., Belokurov V., Maiolino R., Monty S., Isobe Y., Kravtsov A., McClymont W., Übler H., 2026b, MNRAS, 545, staf2110
Ji X., et al., 2026c, MNRAS, 545, staf2235
Johnson B. D., Leja J., Conroy C., Speagle J. S., 2021, ApJS, 254, 22
Johnson B., et al., 2023, dfm/python-fsps: v0.4.4, doi:10.5281/zenodo.8230430
Jones E., Oliphant T., Peterson P., et al., 2001, SciPy: Open source scientific tools for Python, http://www.scipy.org/
Jones B. L., et al., 2025, arXiv e-prints, p. arXiv:2510.07376
Joye W. A., Mandel E., 2003, in Payne H. E., Jedrzejewski R. I., Hook R. N., eds, Astronomical Society of the Pacific Conference Series Vol. 295, Astronomical Data Analysis Software and Systems XII. p. 489
Juodžbalis I., et al., 2024, MNRAS, 535, 853
Juodžbalis I., et al., 2026a, MNRAS, 546, stag086
Juodžbalis I., et al., 2026b, Nature, 653, 1017
Kartje J. F., Königl A., 1991, ApJ, 375, 69
Kido D., Ioka K., Hotokezaka K., Inayoshi K., Irwin C. M., 2025, MNRAS, 544, 3407
Kishimoto M., Antonucci R., Blaes O., 2003, MNRAS, 345, 253
Kishimoto M., Antonucci R., Boisson C., Blaes O., 2004, MNRAS, 354, 1065
Kishimoto M., Antonucci R., Blaes O., 2005, MNRAS, 364, 640
Kishimoto M., Antonucci R., Blaes O., Lawrence A., Boisson C., Albrecht M., Leipski C., 2008, Nature, 454, 492
Kocevski D. D., et al., 2025, ApJ, 986, 126
Kollatschny W., Zetzl M., 2013, A&A, 549, A100
Labbe I., et al., 2024, arXiv e-prints, p. arXiv:2412.04557
Lambrides E., et al., 2025, arXiv e-prints, p. arXiv:2509.09607
Lambrides E., et al., 2026a, arXiv e-prints, p. arXiv:2604.25991
Lambrides E., et al., 2026b, Nature Astronomy, 10, 868
Lamers H. J. G. L. M., Zickgraf F.-J., de Winter D., Houziaux L., Zorec J., 1998, A&A, 340, 117
Laor A., 2006, ApJ, 643, 112
Laor A., Netzer H., Piran T., 1990, MNRAS, 242, 560
Leung G. C. K., et al., 2025, ApJ, 992, 26
Lin X., et al., 2026, ApJ, 997, 364
Lira P., et al., 2021, MNRAS, 507, 579
Liu H., Jiang Y.-F., Quataert E., Greene J. E., Ma Y., 2025, ApJ, 994, 113
Liu Z., et al., 2026, arXiv e-prints, p. arXiv:2604.13000
Lumsden S. L., Moore T. J. T., Smith C., Fujiyoshi T., Bland-Hawthorn J., Ward M. J., 1999, MNRAS, 303, 209
Luridiana V., Morisset C., Shaw R. A., 2015, A&A, 573, A42
Madau P., Maiolino R., 2026, arXiv e-prints, p. arXiv:2602.22386
Madau P., Maiolino R., Scholtz J., D'Eugenio F., 2026, arXiv e-prints, p. arXiv:2604.04216
Maiolino R., Marconi A., Salvati M., Risaliti G., Severgnini P., Oliva E., La Franca F., Vanzi L., 2001, A&A, 365, 28
Maiolino R., et al., 2024, A&A, 691, A145
Maiolino R., et al., 2025, MNRAS, 538, 1921
Matthee J., et al., 2024, ApJ, 963, 129
Matthee J., et al., 2026, arXiv e-prints, p. arXiv:2603.17667
Mazzolari G., et al., 2026, A&A, 706, A372
McClymont W., et al., 2026, MNRAS, 545, staf2092
McLean I. S., 1979, MNRAS, 186, 265
Miller J. S., Goodrich R. W., Mathews W. G., 1991, ApJ, 378, 47
Moran E. C., Barth A. J., Kay L. E., Filippenko A. V., 2000, ApJ, 540, L73
Nagao T., Marconi A., Maiolino R., 2006, A&A, 447, 157
Naidu R. P., et al., 2025, arXiv e-prints, p. arXiv:2503.16596
Naidu R. P., et al., 2026, arXiv e-prints, p. arXiv:2606.30711
Nandal D., Loeb A., 2026, ApJ, 998, 124
Ortame G., Bourne M. A., Koudmani S., Sijacki D., D'Eugenio F., Maiolino R., 2026, arXiv e-prints, p. arXiv:2603.00241
Oudmaijer R. D., Drew J. E., 1999, MNRAS, 305, 166
Pacucci F., Loeb A., 2024, ApJ, 964, 154
Pacucci F., Ferrara A., Kocevski D. D., 2026, arXiv e-prints, p. arXiv:2601.14368
Pasha I., Miller T. B., 2023, The Journal of Open Source Software, 8, 5703
Pérez-González P. G., et al., 2026, arXiv e-prints, p. arXiv:2602.20247
Planck Collaboration 2015, A&A, 576, A104
Planck Collaboration 2020, A&A, 641, A12
Planck Collaboration et al., 2020, A&A, 641, A6
Ramos Almeida C., Martínez González M. J., Asensio Ramos A., Acosta-Pulido J. A., Hönig S. F., Alonso-Herrero A., Tadhunter C. N., González-Martín O., 2016, MNRAS, 461, 1387
Ronayne K., et al., 2026, ApJ, 1003, 234
Rupke D. S., Veilleux S., Sanders D. B., 2005, ApJS, 160, 87
Rusakov V., et al., 2026, Nature, 649, 574
Schlafly E. F., Finkbeiner D. P., 2011, ApJ, 737, 103
Scholtz J., et al., 2025, arXiv e-prints, p. arXiv:2510.01034
Scholtz J., et al., 2026, arXiv e-prints, p. arXiv:2603.22277
Serkowski K., Mathewson D. S., Ford V. L., 1975, ApJ, 196, 261
Setton D. J., et al., 2025a, ApJ, 991, L10
Setton D. J., et al., 2025b, ApJ, 995, 118
Simmonds C., Bauer F. E., Thuan T. X., Izotov Y. I., Stern D., Harrison F. A., 2016, A&A, 596, A64
Smith P. S., Schmidt G. D., Allen R. G., Angel J. R. P., 1995, ApJ, 444, 146
Smith J. E., Young S., Robinson A., Corbett E. A., Giannuzzo M. E., Axon D. J., Hough J. H., 2002, MNRAS, 335, 773
Smith J. E., Robinson A., Alexander D. M., Young S., Axon D. J., Corbett E. A., 2004, MNRAS, 350, 140
Smith J. E., Robinson A., Young S., Axon D. J., Corbett E. A., 2005, MNRAS, 359, 846
Sneppen A., et al., 2026a, arXiv e-prints, p. arXiv:2601.18864
Sneppen A., et al., 2026b, arXiv e-prints, p. arXiv:2604.09399
Sun W. Q., et al., 2026, The Open Journal of Astrophysics, 9, 62505
Taylor M. B., 2005, in Shopbell P., Britton M., Ebert R., eds, Astronomical Society of the Pacific Conference Series Vol. 347, Astronomical Data Analysis Software and Systems XIV. p. 29
Taylor A. J., et al., 2025, ApJ, 986, 165
Torralba A., et al., 2026, A&A, 707, A75
Tran H. D., 1995, ApJ, 440, 565
Tran H. D., 2003, ApJ, 583, 632
Tripodi R., et al., 2025, ApJ, 994, L6
Urry C. M., Padovani P., 1995, PASP, 107, 803
Véron-Cetty M.-P., Joly M., Véron P., 2004, A&A, 417, 515
Vink J. S., Drew J. E., Harries T. J., Oudmaijer R. D., 2002, MNRAS, 337, 356
Wang B., et al., 2024, ApJ, 969, L13
Wang B., et al., 2025, ApJ, 984, 121
Wang B., et al., 2026, ApJ, 1003, 10
Wardle J. F. C., Kronberg P. P., 1974, ApJ, 194, 249
Whittet D. C. B., Martin P. G., Hough J. H., Rouse M. F., Bailey J. A., Axon D. J., 1992, ApJ, 386, 562
Yang C., et al., 2025, ApJ, 995, L44
Young S., Hough J. H., Axon D. J., Bailey J. A., Ward M. J., 1995, MNRAS, 272, 513
Yue M., Eilers A.-C., Ananna T. T., Panagiotou C., Kara E., Miyaji T., 2024, ApJ, 974, L26

Zhang Z., Jiang L., Liu W., Ho L. C., 2025, ApJ, 985, 119
Zickgraf F.-J., Wolf B., Stahl O., Leitherer C., Klare G., 1985, A&A, 143, 421
Zickgraf F. J., Wolf B., Stahl O., Leitherer C., Appenzeller I., 1986, A&A, 163, 119
Zucchi G., Ji X., Madau P., Maiolino R., Juodžbalis I., D'Eugenio F., Geris S., Isobe Y., 2026, A&A, 707, A52
de Graaff A., et al., 2025, A&A, 701, A168
van Rossum G., 1995, CWI Technical Report, CS-R9526

APPENDIX A: OFF-TARGET NULL SPECTRA

As an independent check on the Stokes-flux noise, we extracted off-target "null" spectra from the same reduced FORS2 two-dimensional products used for the science spectrum. For each of the eight retained OBs, we placed two apertures above and below the target trace, offset by 24 spatial pixels from the ordinary and extraordinary target positions. Each aperture had the same half-width of 8 pixels used for the corresponding beam extraction. We then formed Stokes-flux spectra directly from the ordinary–extraordinary beam differences, producing 16 null realisations in total.

Fig. A1 compares the null spectra with the science Stokes-flux products. The median null spectra remain close to zero across the wavelength range, including the H α region. As reference noise level, we use the robust null scatter $\sigma_{\rm R}(\lambda)$, defined in each wavelength bin as 1.4826 times the median absolute deviation of the 16 null realisations. This procedure estimates their standard deviation while remaining insensitive to outliers. In the continuum window 5200–6400 Å, the median absolute null residuals are only 0.22 times the robust null scatter $\sigma_{\rm R}$ in both Q and U. Across the H α window 6400–6620 Å, the corresponding values are 0.23 in both Stokes components, and in the line-core window 6500–6625 Å they are 0.23 and 0.25 for Q and U, respectively. We therefore find no evidence for a coherent off-source Stokes residual that could mimic the line signal.

The empirical null scatter is also smaller than the propagated Stokes-flux errors used in the science analysis: for both Q and U, the median ratios between the null scatter and the propagated error are 0.69 in the continuum window, and 0.57 across broad H α. The mismatch is by construction, since the null apertures contain no photon noise. Indeed, the null-to-propagated noise ratio decreases where the science intensity rises (Spearman $\rho = -0.33$ between $I/I_{\rm cont}$ and the mean Q, U ratio).

APPENDIX B: ALTERNATIVE AVERAGING SCHEMES

The polarisation values we report are sensitive to the averaging method and weighting scheme employed. Here we discuss the implications for our analysis. Contrary to expectations, inverse-variance weighting (IVW) gives noisier averages. This was inferred by taking u and q and by comparing their standard deviation across line-free spectral regions between the IVW average and the standard unweighted average.

In addition, we also employ the median instead of the mean when performing adaptive binning. The mean is nominally more appropriate than the median for linear quantities such as U and Q. However, when binning the data with fixed bin size, we noticed increased noise compared to the median-averaged bins, hence we resorted to using the median everywhere, i.e. also for the adaptively binned data. When estimating the uncertainties, we upscale the variance by the canonical value of $\pi/2$, to account for the larger uncertainties of the median relative to the mean.

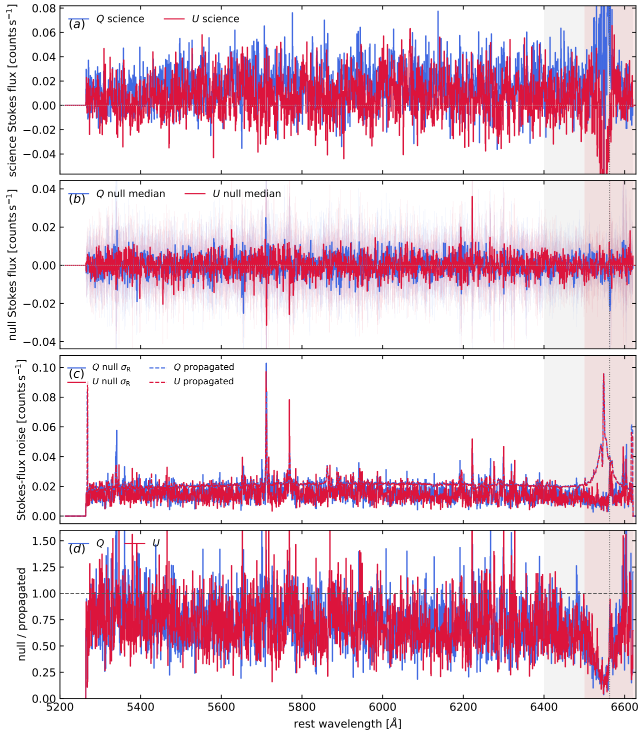

Figure A1. Off-target null-spectrum check in Stokes flux. Panel (a) shows the median science Q and U spectra. Panel (b) shows the median off-target null spectra, with shaded bands marking the robust scatter of the 16 null realisations. Panel (c) compares the robust null scatter with the propagated Stokes-flux errors used for the science spectrum. Panel (d) shows their ratio; values below unity indicate that the off-source empirical noise is smaller than the propagated error. The grey band marks the blue wing of broad H α, while the red band is the main line.

Crucially, we verified that neither using IVW instead of unweighted, nor employing the mean instead of the median affects our main results, with the difference being $\lesssim 0.1$ per cent, below our fiducial systematics floor of $\simeq 0.4$ per cent (set by the unknown foreground polarisation, Section 2). We tested that any differences are not due to outliers, since σ-clipping the data has negligible effect on the stacks and binning.

Regardless of the method, we find that broad H α is still less polarised than the continuum and with a different angle, and the polarised-flux spectrum still peaks at H α. There is, however, a difference in the polarisation colour. The continuum-colour fit is somewhat steeper than for the fiducial median stack, with $dp/d\lambda = -0.41 \pm 0.12$ per cent per 1000 Å (3.5 σ), driven primarily by the steeper $dq/d\lambda = -0.35 \pm 0.12$ per cent per 1000 Å. The resulting index difference is $\Delta\beta = -1.31 \pm 0.42$ (3.1 σ). We thus warn that the grey polarisation spectrum is not a foregone conclusion.

APPENDIX C: FLUX-ONLY ELECTRON-SCATTERING MODEL

Here we show the best-fit model obtained by removing polarisation from the model described in Section 3.6 and therefore fitting the model only to the total-intensity spectrum. The best-fit spectrum is rendered in Fig. C1a, which we find indistinguishable from the spectrum of Fig. 7a. Crucially, the fit residuals (Fig. C1b) show the same high-significance undulations we reported in Fig. 7b, demonstrating

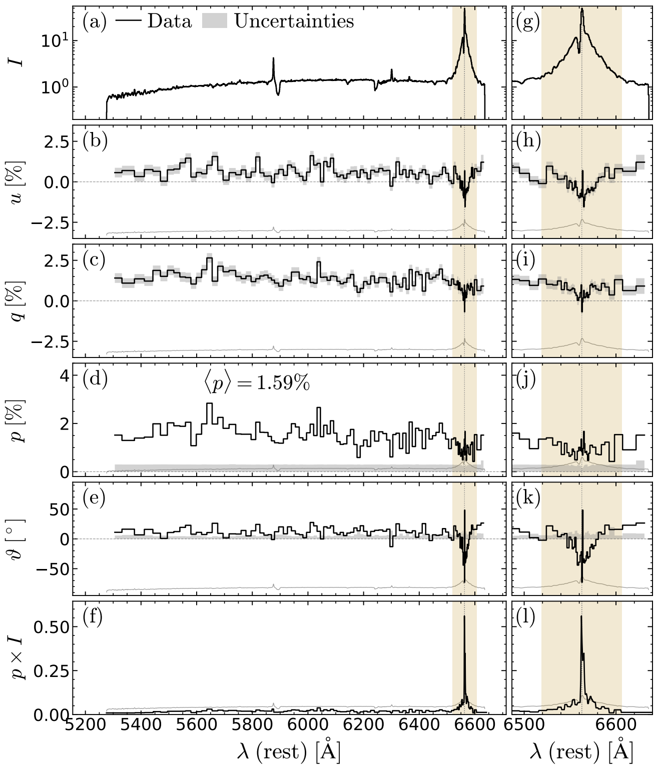

Figure B1. Adaptive-binning spectropolarimetry using a clipped-mean stack, shown as a robustness comparison to Fig. 2. The qualitative behaviour is unchanged, but the polarisation colour becomes bluer, as described in the text.

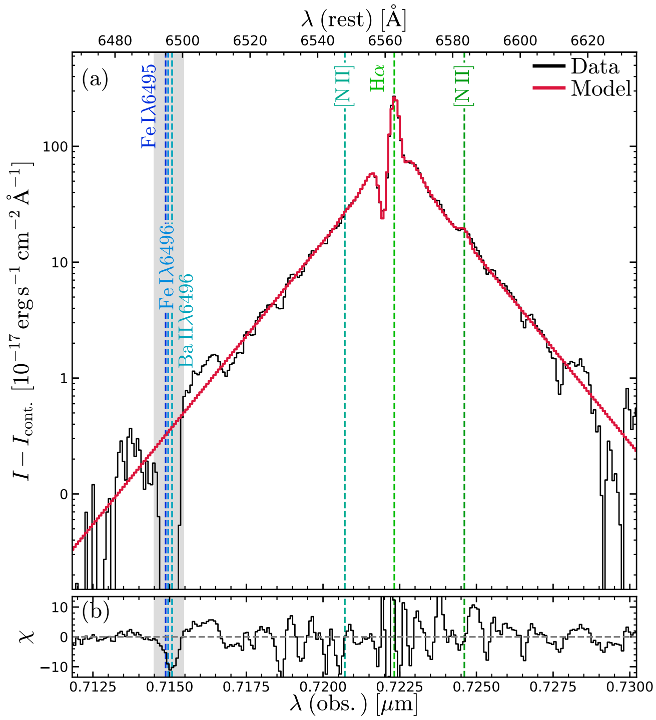

Figure C1. Same as Fig. 7, but fitting only Stokes I, without the polarisation data. The similarity of the residual structure to that in Fig. 7 shows that the dominant model mismatch is already present in the flux spectrum itself.

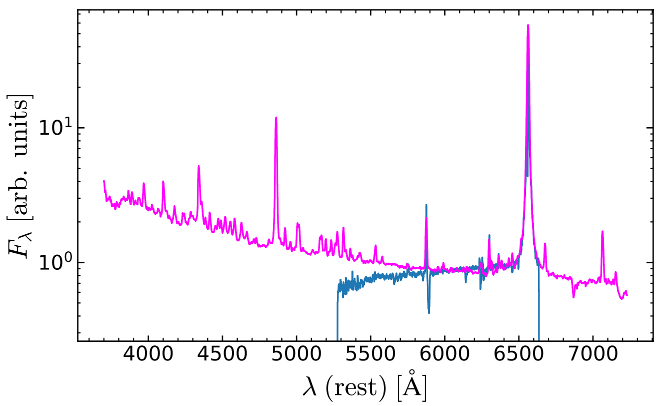

Figure D1. Comparison of J1025 to HD 51585; there are many similarities and differences, but some of the similarities are in rather peculiar properties, such as auroral-line emission and Balmer-line properties.

that the data–model mismatch reported in Section 3.6 is not driven by the inclusion of p in the toy model, but is intrinsic to the spectral flux density, which is the only quantity we model here.

APPENDIX D: THE CURIOUS CASE OF STAR HD 51585

In addition to the eponymous emission lines, Herbig Be and B[e] stars also display other characteristics in common with LRDs, such that it is instructive to study them. Of course, these stars can scarcely be considered a homogeneous family, bar the defining presence of a blue continuum and prominent emission lines. For example, the archetypal Herbig Be star γ Cas has low-EW H α ($\simeq -25$ Å) with a narrow line profile dominated by rotation (equatorial velocity $v_{\rm eq} \simeq 450$ km s^{-1}; Archer et al. 2025). To add to the mismatch, γ Cas is also a strong source of thermalised X-rays (possibly arising from the interaction between the stellar atmosphere and the surrounding decretion disc).

However, in some members of this peculiar class of stars, the spectral similarities with LRDs are much stronger. The B[e] star HD 51585 (Fig. D1) is a case in point. This compact, post-AGB planetary-nebula B[e] star (cPNB[e]; Lamers et al. 1998) is thought to be undergoing a rapid transition phase towards a true PN. It shows prominent H α with $EW(\text{H}\,\alpha) \simeq -900$ Å (Jaschek et al. 1996), higher than many LRDs (cf. −340 Å for J1025; Ji et al. 2026c). The continuum-subtracted line profile displays the same exponential-like wings as in J1025 (Fig. D1b), and the Balmer decrement is $F(\text{H}\,\alpha)/F(\text{H}\,\beta) \simeq 6$, despite the remarkably blue continuum colour. As for other emission lines, HD 51585 displays extremely high auroral-to-strong emission-line ratios ([S II]λλ4069,4071,6731 vs [S II]λλ6716,6731, [N II]λ5755 vs [N II]λ6583, [O III]λ4363 vs [O III]λ5007) also seen in some well-studied LRDs at both low and high redshifts (e.g., Ji et al. 2026c and D'Eugenio et al. 2025), which some authors consider evidence for a two-zone density structure (D'Eugenio et al. 2025). The forest of permitted Fe II and forbidden [Fe II] emission is also worth mentioning (cf. Jaschek et al. 1996 and Lin et al. 2026; Tripodi et al. 2025; Ji et al. 2026c; Torralba et al. 2026; D'Eugenio et al. 2025; Lambrides et al. 2025).

Another suggestive parallel between LRDs and B[e] stars is represented by the classic Zickgraf B[e]-star picture (Zickgraf et al. 1985, 1986): a fast, highly ionized polar wind plus a slow, dense equatorial outflow. According to Zickgraf et al. (1985), this model can produce most of the peculiar spectral features seen in B[e] stars and, therefore, in LRDs (Fig. D1). Translated to an AGN, the polar component would provide an ionized scattering channel for the continuum and broad lines, while the denser equatorial flow would dominate low-ionization line formation and obscuration, giving rise, e.g., to metal and Balmer absorption. In such a geometry the continuum can be polarised mainly by the polar component, yet broad H α can be only weakly polarised if most of the line photons are produced in a larger region than the disc. The Zickgraf-style two-component outflow provides a useful phenomenological template for an LRD in which a fast ionized polar medium and a slower dense equatorial medium coexist, echoing the models of Sneppen et al. (2026a) and Matthee et al. (2026).